Elsevier Editorial System(tm) for Earth and Planetary Science Letters

Manuscript Draft

Manuscript Number: EPSL-D-17-00839R2

Title: Sedimentary evidence for enhanced hydrological cycling in response to rapid carbon release during the early Toarcian oceanic anoxic event

Article Type: Letters

Keywords: Toarcian, carbon isotope, hydrological cycling, sedimentology, atmospheric warming

Corresponding Author: Dr. Kentaro Izumi,

Corresponding Author's Institution: Chiba University

First Author: Kentaro Izumi

Order of Authors: Kentaro Izumi; David B Kemp; Shoma Itamiya; Mutsuko Inui

Abstract: A pronounced excursion in the carbon-isotope composition of biospheric carbon and coeval seawater warming during the early Toarcian (~183 Ma) has been linked to the large-scale transfer of 12C-enriched carbon to the oceans and atmosphere. A European bias in the distribution of available data means that the precise pattern, tempo and global expression of this carbon cycle perturbation, and the associated environmental responses, remain uncertain. Here, we present a new cm-scale terrestrial-dominated carbon-isotope record through an expanded early Toarcian section from Japan that displays a negative excursion pattern similar to marine and terrestrial carbon-isotope records documented from Europe. These new data suggest that 12C-enriched carbon was added to the biosphere in at least one rapid, millennial-scale pulse. Sedimentological analysis indicates a close association between the carbon-isotope excursion and high-energy sediment transport and enhanced fluvial discharge. Together, these data support the hypothesis that a sudden strengthening of the global hydrological cycle occurred in direct and immediate response to rapid carbon release and atmospheric warming.

CHIBA UNIVERSITY

Dr. Kentaro Izumi
Faculty & Graduate School of Education
Chiba University
1-33 Yayoi-cho, Inage-ku, Chiba-shi
Chiba 263-8522, Japan
Tel. +43-290-3682
e-mail: izumi@chiba-u.jp

10/10/17

FAO: The Editor, *Earth and Planetary Science Letters*

Re: Revision of EPSL-D-17-00839R1 - "Sedimentary evidence for enhanced hydrological cycling in response to rapid carbon release during the early Toarcian oceanic anoxic event"

Dear Prof. Vance,

Please find accompanying this letter a revision of the above manuscript that was recently reviewed for *Earth and Planetary Science Letters*. We have detailed below the changes made to our manuscript in response to the comments raised by the Editor. We provide two copies of the manuscript: one with track changes with our revisions highlighted, and one clean copy.

We are delighted that the submission has been judged of sufficient quality for publication in *Earth and Planetary Science Letters* after minor revision. In our revision, we have addressed all the issues raised by the Editor, and we have outlined below detailed responses to all comments.

Editor

Thank you for the revision and for attending to the reviewer comments. I have read the revision. The only things that now need looking at, I think, are some very minor suggestions I have made for better phrasing - which you are welcome to take or leave. I have marked these on a hard copy and will send a scan of this to you by separate e-mail.

Please could you attend to these final points, and then we should be able to accept it for publication.

=> Thank you very much for your thoughtful editing. During revision, we changed the manuscript as suggested by your comments.

Yours sincerely,

Kentaro Izumi, David B. Kemp, Shoma Itamiya, and Mutsuko Inui

Sedimentary evidence for enhanced hydrological cycling in response to rapid carbon release during the early Toarcian oceanic anoxic event

Kentaro Izumi[a, *], David B. Kemp[b], Shoma Itamiya[c], and Mutsuko Inui[c]

[a]*Faculty & Graduate School of Education, Chiba University, 1-33 Yayoi-cho, Inage-ku, Chiba-shi, Chiba 263-8522, Japan*

[b]*School of Geosciences, University of Aberdeen, Old Aberdeen, Aberdeen, AB24 3UE, UK*

[c]*School of Science and Engineering, Kokushikan University, 4-28-1 Setagaya, Setagaya-ku, Tokyo 154-8515, Japan*

*Corresponding author at: Faculty & Graduate School of Education, Chiba University, Chiba, Japan.

E-mail address: izumi@chiba-u.jp (K. Izumi).

ABSTRACT

A pronounced excursion in the carbon-isotope composition of biospheric carbon and coeval seawater warming during the early Toarcian (~183 Ma) has been linked to the large-scale transfer of ^{12}C-enriched carbon to the oceans and atmosphere. A European bias in the distribution of available data means that the precise pattern, tempo and global expression of this carbon cycle perturbation, and the associated environmental responses, remain uncertain. Here, we present a new cm-scale

terrestrial-dominated carbon-isotope record through an expanded early Toarcian section from Japan that displays a negative excursion pattern similar to marine and terrestrial carbon-isotope records documented from Europe. These new data suggest that ^{12}C-enriched carbon was ~~effused~~ added to the biosphere in at least one rapid, millennial-scale pulse. Sedimentological analysis indicates a close association between the carbon-isotope excursion and high-energy sediment transport and enhanced fluvial discharge. Together, these data support the hypothesis that a sudden strengthening of the global hydrological cycle occurred in direct and immediate response to rapid carbon release and atmospheric warming.

Keywords: Toarcian, carbon isotope, hydrological cycling, sedimentology, atmospheric warming

1. Introduction

The widespread occurrence of organic-rich facies deposited under reducing conditions during the early Toarcian has led to the recognition of one of the most pronounced oceanic anoxic events (OAEs) of the Phanerozoic. Broadly contemporaneous with deoxygenation is evidence for abrupt warming (Bailey et al., 2003), an increase in continental chemical weathering rates (Brazier et al., 2015; Cohen et al., 2004; Percival et al., 2016; Them et al., 2017a), and changes in atmospheric pCO_2 (McElwain et al., 2005). The major sedimentary reservoirs of carbon at this time record a 3-7‰ negative excursion in carbon-isotopes ($\delta^{13}C$), indicative of a large input of ^{12}C-enriched carbon (Hesselbo et al., 2000; Kemp et al., 2005; Svensen et al., 2007). Carbon-isotope records from Boreal and Tethyan sections

~~sometimes~~ often show that the overall shift to minimum values was stepped, comprising at least two rapid negative shifts in $\delta^{13}C$ superimposed on a more protracted decrease (e.g. Bodin et al., 2016; Hermoso et al., 2009; Hesselbo and Pienkowski, 2011; Jenkyns et al., 2001; Kemp et al., 2005; Ruebsam et al., 2004; Suan et al., 2015).

This $\delta^{13}C$ morphology has not yet been convincingly replicated outside of the Boreal and Tethyan realms, although recent work by Them et al. (2017b) indicates evidence for a complex and possibly stepped structure to the ~~excursion~~ onset of the excursion in North America (Eastern Panthalassa Ocean). Establishing the precise pattern, reproducibility and magnitude of the early Toarcian $\delta^{13}C$ excursion is of central importance for determining the ultimate cause(s) of the event and associated environmental change. Similarly, there is a lack of data elucidating the environmental responses to inferred carbon release from globally distributed settings. These issues limit our understanding of the effects (both local and global) of carbon-forced greenhouse warming, and hence the role that events like the early Toarcian can play as analogues for modern day C release scenarios. To address these issues, we have conducted a high-resolution organic carbon-isotope and sedimentological analysis of an expanded early Toarcian succession from Japan that was deposited at the margin of the Panthalassa Ocean (Fig. 1).

2. Geological setting

Lower Toarcian organic-rich mudstones, siltstones and fine-grained sandstones of the Nishinakayama Formation (Toyora Group) crop out in the Toyora area of southwest Japan, Yamaguchi prefecture (Fig. 1). The rocks form part of the fill

of the Tabe Basin. A long history of research on the Sakuraguchi-dani stream bed succession (131° 03'E 34° 08'E; Fig. 1) has revealed a rich ammonite fauna, allowing demarcation of the lower Toarcian (Nakada and Matsuoka, 2011 and references therein). Recent geochemical analysis of the succession has demonstrated that the early Toarcian carbon cycle perturbation is well expressed, with a ~3‰ negative excursion recorded in organic carbon-isotopes spanning ~30 m (Izumi et al., 2012; Kemp and Izumi, 2014).

3. Analytical methods

3.1. Carbon isotope analysis

For this study, 80 mudstone samples were collected, primarily across the ~5 m interval comprising the onset of the excursion, and analysed for ~~organic~~ the $\delta^{13}C$ of organic carbon~~composition~~. In addition, $\delta^{13}C$ analysis was also carried out on 6 macrofossil wood samples. For mudstone and wood $\delta^{13}C$ measurements, powdered samples were decalcified in 3M HCl (heated to 60°C for 3 hours in the case of wood samples to help remove pyrite) and then washed with deionised water until neutrality was reached. After drying, samples were weighed into tin capsules and analysed on a Europa Scientific 20/20 mass spectrometer (rock samples) or a Thermo Scientific MAT253 isotope ratio mass spectrometer (wood samples). Precision for both instruments was quantified ~~from~~ via analysis of standards, and was better than 0.2‰.

3.2. Rock-Eval analysis

Organic matter was characterised by Rock-Eval pyrolysis of 5 mudstone samples. Rock-Eval pyrolysis was carried out on 5 powdered samples distributed through the succession using a Rock-Eval 6 apparatus (Vinci Technologies), run in 'Basic Method' mode (see Behar et al., 2001). Both the S1 and S2 signals were successively determined with flame ionization detection. The S1 signal corresponds to the amount of free hydrocarbons volatilized for 3 min at 300 °C, and the S2 signal represents the amount of hydrocarbons generated from kerogen cracking between 300 ~~to~~ and 650 °C with a heating rate of 25 °C per 1 min. The amount of CO_2 generated between 300 and 400 °C was determined as the S3 signal, with infrared detection. All parameters (S1, S2, and S3) are expressed in mg of hydrocarbons or CO_2 per gram of rock. T_{max} is the temperature at which the maximum hydrocarbon yield resulting from kerogen cracking occurs. Residual organic carbon contents of the pyrolyzed samples were obtained by combustion in air from 300 to 650 °C, with a heating rate of 20 °C per 1 min. The CO_2 and CO resulting from this combustion was also determined with an infrared cell, and corresponds to peak~~s~~ S4CO_2 for CO_2 and peak S4CO for CO. By using these parameters with the S1 to S3 signals, the total organic carbon (TOC) content (wt.%) was calculated as the sum of pyrolyzed and residual organic carbon. The hydrogen index (HI, mg HC/g TOC) and oxygen index (OI, mg CO_2/g TOC) were calculated as S2/TOC, and S3/TOC, respectively.

For the application of Rock-Eval pyrolysis to the Toarcian sediments with basic interpretations, see Röhl and Schmid-Röhl (2005) for instance.

3.3. Sedimentological analysis

123 The sedimentology of the entire succession was investigated based on thin-
124 section study of 72 mudstone samples, and polished/cut surface study of 28 sandstone
125 samples. All thin-section observations were carried out ~~by~~ using a polarizing
126 microscope (BX-51, Olympus) at Kokushikan University. In this study, silt beds are
127 defined as silty layers with internal silty laminae, whereas a silt lamina is the smallest
128 macroscopic layer without internal layering. Silt lamina thicknesses were measured
129 from thin-section scanned images (jpeg format), using ImageJ image-processing
130 software. Thin-section scanned images were obtained using a film scanner (KFS-
131 1400, Kenko film scanner) that is equipped with polarizers. For thickness
132 measurement of individual silt laminae, only distinct and continuous silt laminae
133 recognised in a scan image were used. In the case of silt lamina whose thickness
134 changes horizontally, the maximum thickness was used. All individual thickness data
135 obtained from the single thin-section scanned image were used when calculating
136 average thickness. Measurements of silt bed thicknesses were carried out in the same
137 way.

138 For sandstone sedimentological analysis, sandstone samples were cut
139 perpendicular to bedding planes and polished if necessary. Such cut or polished
140 surfaces were scanned using a flatbed image scanner (GT-X770, EPSON). For one
141 sandstone sample (Sample ID: 2016-S1-SST5), grain-size analysis was conducted in
142 order to investigate the detailed sedimentary features that are difficult to identify by
143 naked-eye observation. Grain-size analysis was based on the method described in
144 Yoshida et al. (1995), which performs measurements of long-axis diameters of
145 monocrystalline quartz grains under thin-section observation. In this study, long-axis
146 diameters of monocrystalline quartz grains were measured in ImageJ using 5 x 5 mm
147 meshed jpeg images of thin-section photomicrographs.

4. Results

4.1. Carbon-isotope data and Rock Eval analysis

Our cm-scale $\delta^{13}C$ analysis of mudstones across the interval comprising the onset of the excursion reveals a steady decrease of ~0.7‰ over the lowermost ~13 m of the succession, from ~-24.8‰ to ~-25.5‰ (Fig. 2). At -4.58 m in the section, a -2.3‰ shift in $\delta^{13}C$ occurs over 21 cm of strata (labelled A on Fig. 2; Table S1 in supplementary materials). This decrease straddles an 18 cm thick horizon of unconsolidated, poorly sorted (clay to pebble sized) mudstone fragments. This is interpreted as a fault breccia (Fig. 2), though the lateral extent of the outcrop (~20 cm) and position within a stream bed prevents a fuller assessment. Ammonite biostratigraphy indicates an early Toarcian age for strata immediately below and above this inferred fault (*P. paltus* Zone, Fig. 2). Above this decrease, $\delta^{13}C$ increases by ~1‰ over the ~~following~~ succeeding ~2 m (Fig. 2). Between -2.59 and -2.33 m, there is a second, broadly defined decrease in $\delta^{13}C$ of -2.2‰ (Fig. 2). This second decrease is interrupted by a positive excursion of ~2.3‰ that occurs over 6 cm, from -2.44 to -2.38 m (Fig. 2). Between -2.38 and -2.33 m, there is a very abrupt negative shift in $\delta^{13}C_{organic}$ of -2.9‰ (labelled B on Fig. 2; Table S1 in supplementary materials). Macrofossil wood $\delta^{13}C$ data broadly track bulk mudstone $\delta^{13}C$ (Fig. 2; Table S1 in Appendix A). Our Rock-Eval results ~~-~~indicate extremely low hydrogen index (i.e. 1 to 3) and oxygen index (i.e. 5 to 23) values (Figure S1 in supplementary material). These data suggest that the organic matter is predominantly Type IV kerogen. It is widely recognized that Type IV kerogen generally consists of oxidised

intertinite of higher plant origin, although it may also consist of oxically degraded, plankton derived, fine-grained, amorphous material (Tyson, 1995). The abundant presence of both macro- and microscopic fossil wood and plant debris (Kemp and Izumi, 2014) suggests that the organic matter in the studied mudstones is indeed dominated by oxidised intertinite of higher plant origin.

4.2. Mudstone sedimentology

Three primary mudstone lithofacies can be identified in the succession: 1) laminated (ranging from well laminated to poorly laminated), 2) bioturbated, and 3) thin-bedded (Fig. 3). Parallel lamination, indicating quiescent and likely oxygen-deficient conditions, is recognised in mudstones throughout the studied interval (see also Izumi et al., 2012). However, our detailed microscopic thin-section analysis also reveals the presence of sedimentary features indicative of advective transport and oxygenated, high-energy conditions. Notably, we recognise cross laminations, irregular silty layers (e.g. wavy or lenticular silt laminae, often with erosional bases), silt beds, fluid-mud layers, putative tempestites/wave enhanced sediment gravity flow deposits, and burrows (Figs. 2 and 3; see also Table S2 in supplementary materials). Among these sedimentary features, fluid-mud layers and putative tempestites/wave enhanced sediment gravity flow deposits are described from the Nishinakayama Formation for the first time. Burrows (e.g. *Phycosiphon*) were recognised throughout the succession (Fig. 2). Crucially, however, sedimentary features indicative of high-energy conditions are concentrated between -4.53 and ~14 m, broadly coincident with the main phase of the $\delta^{13}C$ excursion (Fig. 2).

The thicknesses of silt laminae measured in thin sections of the mudstone facies vary through the studied interval (from 0.08 to 0.849 mm, mean 0.26 mm; see also Table S2 in supplementary materials). Between -16.02 and -4.53 m, silt laminae are of broadly consistent thickness (~0.2 mm). At -4.46 m, and coincident with the onset of the $\delta^{13}C$ excursion, silt laminae thicknesses increase and show greater variability (Fig. 2). Thicknesses remain highly variable through the main phase of the $\delta^{13}C$ excursion between -4.46 m and ~10 m. Average thickness and variability decreases between ~10 m and ~25 m, coeval with decreasing $\delta^{13}C$ (Fig. 2). Laminae thicknesses are broadly stable between ~25 m and 50 m (Fig. 2).

4.3. Sandstone sedimentology

Sandstone beds are concentrated between ~0 and ~7 m within the main phase of the $\delta^{13}C$ excursion (Fig. 2), and have previously been interpreted as turbidites (Kawamura, 2010). Based on detailed observation of sandstone cut and polished surfaces of 28 samples, however, three types of sediment gravity flow deposits were identified: turbidites (16 samples), debrites (9 samples), and hyperpycnites (3 samples). Most notably, debrites (Fig. 3I) and hyperpycnites (Figs. 3H and 4) are described from the Nishinakayama Formation for the first time. The recognition of hyperpycnites, which are formed by hyperpycnal flows generated by river floods (Mulder and Alexander, 2001; Mulder et al., 2001, 2003), is especially important for palaeoclimatic ~~implications, which is~~interpretations as discussed below (see section 5.2).

5. Discussion

222

223 *5.1. Evidence for rapid carbon release during the Early Toarcian*

224

225 Rock-Eval data (Fig. S1), coupled with the similarity between the mudstone
226 and macrofossil wood $\delta^{13}C$ data (Fig. 2), emphasizes the dominantly terrestrial nature
227 of the organic matter in the Sakuraguchi-dani succession (see also Kemp and Izumi,
228 2014). Hence, ~~The~~ the bulk mudstone $\delta^{13}C$ data in the succession ~~hence~~
229 predominantly reflect the composition of CO_2 in the early Toarcian atmosphere. Two
230 negative shifts are present across the onset of the $\delta^{13}C$ excursion in the succession
231 (labeled A and B, -2.3‰ and -2.9‰ respectively, Fig. 2). The magnitude of these
232 shifts is comparable to the magnitude of similar and correlable shifts recognised in
233 marine and terrestrial organic matter from European successions (~1-4‰, see also
234 Fig. 5). The veracity of shift A cannot be ascertained, and its brevity is almost
235 certainly a consequence of the inferred fault. Nevertheless, $\delta^{13}C$ values immediately
236 below and above the inferred fault-related brecciated interval at shift A show
237 increasing trends (Fig. 2), and thus a negative shift of uncertain brevity (though
238 spanning less than one ammonite Zone) must have occurred between deposition of the
239 strata preserved below and above the inferred fault.

240 There is no sedimentological evidence for a fault or break in sedimentation
241 across the larger, second negative $\delta^{13}C$ shift beginning at -2.38 m (shift B, Fig. 2).
242 This shift corresponds to <0.15% of the sandstone-free thickness of the overall
243 excursion (~5 cm versus ~34 m). Considering a timescale of ~500-900 k.y. for the
244 excursion as a whole (Boulila et al., 2014; Suan et al., 2008), and notwithstanding
245 mixing/residence time~~s~~ constraints on the expression of $\delta^{13}C$ changes and
246 sedimentation rate variations, shift B likely has a millennial-scale duration (~0.7-1.3

k.y.). This is consistent with Kemp et al. (2005), who described similarly stratigraphically abrupt shifts in $\delta^{13}C$ from Yorkshire, UK. Although rapid $\delta^{13}C$ changes in the early Toarcian very likely occurred within the context of more protracted C ~~effusion~~ emission and warming from volcanic CO_2 sources (e.g. Kemp et al., 2005; Svensen et al., 2007; Suan et al., 2008), our findings emphasise the global nature and rapidity of these changes. Our data thus implicitly support a rapid, global C release mechanism such as hydrate dissociation (e.g. Hesselbo et al., 2000; Kemp et al., 2005).

5.2. Sedimentary features indicative of enhanced fluvial discharge and energetic bottom conditions: identification and palaeoclimatic implications

5.2.1. Fluid-mud deposit layers

Thin-section analysis of silty mudstones reveals the presence of distinct thin (~mm scale) muddy layers, whose lithofacies differ from that of surrounding silty mudstones with parallel-laminated lithofacies (Fig. 3A). The general lithofacies of these distinct thin muddy layers is characterized by: 1) homogeneous internal structure with no or very rare presence of faint laminations, 2) sharp bed contacts, 3) lack of bioturbation, and 4) relatively finer-grained composition with randomly scattered amorphous organic debris (Fig. 3D, E). The lithofacies of these thin muddy layers match those described previously in fluid-mud deposits (Dalrymple et al., 2003).

A fluid mud is defined as a high-density, bottom-hugging mobile subaqueous body of fine-grained suspended-sediment with a concentration of > 10g/L (Faas,

1991). Fluid mud is composed primarily of clay- to silt-sized particles with variable amounts of organic matter (Dalrymple et al., 2003). On the basis of recent experiments and observations, fluid-mud deposits are characterized by: 1) homogeneous and structureless muddy layers (e.g. lack of internal laminations and grading), 2) sharp basal contacts, 3) rare bioturbation, 4) aggregates of clay particles in face-to-face contact with each other (FF-aggregates), and 5) initial thickness of > ~1 cm (Dalrymple et al., 2003; Nishida et al., 2013). Among these characteristics, FF aggregates can be destroyed by sediment diagenesis and thus may not be recognized in lithified strata, although they are preserved in historical layers in modern core samples and young (i.e. Quaternary) records (Nishida and Ito, 2009; Nishida et al., 2013).

With respect to thickness of fluid-mud deposits, it is generally considered that >~1 cm (>~5 mm after compaction) is ~~used as~~ a minimum thickness to distinguish fluid-mud layers from other muddy layers that accumulated by slow, particle-by-particle settling from suspension (Ichaso and Dalrymple, 2009). Although distinct muddy layers recognized within the silty mudstones of the Nishinakayama Formation are very similar to fluid-mud deposits, in most cases their thicknesses are <5 mm. Nevertheless, estimation of the minimum thickness of fluid-mud deposit layers in ancient strata by Ichaso and Dalrymple (2009) was not supported by data. According to a recent study estimating the degree of mudstone compactional thinning (Izumi et al., 2017), mudstones with low Ca abundances are generally affected more by mechanical compaction than Ca-rich mudstones. Mudstones of the Nishinakayama Formation have very low Ca abundances (0.21 to 5.99 wt.% as CaO; Tanabe et al., 1982), and therefore may have been ~~largely~~ greatly affected by mechanical compaction, resulting in >~70 % thinning according to the empirical relationship

between the degree~~s~~ of mudstone compactional thinning and CaO abundances (Izumi et al., 2017). It is also important to emphasize that the empirical relationship ~~by~~ of Izumi et al. (2017) ~~shows~~ has a l~~arge range of the~~wide 95% confidence interval, and that the degree of compactional thinning of the ~~recognized~~ muddy layers from the Nishinakayama Formation might have reached >~90 % (upper limit of 95% confident interval).

Based on the considerations above, we suggest that the distinct muddy layers from the Nishinakayama Formation are compacted fluid-mud deposit layers. Because the Nishinakayama Formation represents fully marine conditions (Tanabe et al., 1982), the inferred fluid-mud deposits were likely formed by either 1) intense wave action generated by storms, or 2) by increased sediment supply due to flood events (Hill et al., 2007; Ichaso and Dalrymple, 2009). Although it is difficult to precisely distinguish these two possibilities, the latter may be more likely in the case of the Nishinakayama Formation because no large-scale hummocky cross stratification ~~is or~~ has been recognized (Kawamura, 2010). Nevertheless, as discussed below (section 5.2.2), sedimentary features of probable storm origin are also recognized from the studied section, and thus at least some proportion of the fluid-mud deposits we recognise could have a storm-related origin.

5.2.2. Putative tempestites/wave enhanced sediment gravity flow deposits

Parallel lamination in mudstones is generally interpreted to indicate continuous sediment accumulation by suspension settling under relatively still and oxygen-depleted bottom environments (Lazar et al., 2015). However, thin-bedded mudstones are normally formed as a result of discontinuous sediment accumulation by

lateral transport in bed load, for instance, under intermittently energetic conditions (Lazar et al., 2015). Based on our observation, thin-bedded silty mudstones only occur between -2.38 to 3.5 m, which corresponds with the middle part of the 'main phase' of the $\delta^{13}C$ excursion (Fig. 2). This suggests that relatively energetic conditions were dominant during the main phase of the $\delta^{13}C$ excursion. Fig. 3G shows an example of a thin-bedded silty mudstone (Sample ID: 2013-5-5). In this case, at least three independent beds can be recognized: a = homogeneous muddy bed, and b & c = silty beds with basal internal laminae showing gradual lithological change (fining upward trend) (Fig. 3G). Bed a is interpreted as fluid-mud deposit layer due to its homogeneous lithofacies, finer-grained (muddy) composition, rare bioturbation structures, and sharp bed boundary. Beds b and c are very similar to wave-enhanced sediment-gravity flow produced beds or tempestite beds (Macquaker et al., 2010). Wave-enhanced sediment-gravity flow beds are a likely product of storm-induced waves, and are generally subdivided into three sub-beds; namely, the basal, middle, and top sub-beds produced by traction transport, sediment-gravity flow, and suspension settling, respectively (Macquaker et al., 2010; Lazar et al., 2015). From the lithofacies point of view, the basal sub-bed represents a laminaset composed of silt-rich and largely homogeneous to slightly graded material (Macquaker et al., 2010; Lazar et al., 2015). The basal sub-bed may not be continuous in some cases, and it has a sharp to gradational top. The basal sub-bed indicates traction transport. The middle sub-bed also represents a laminaset composed of multiple, very thin broadly curved to wavy laminae composed of silt grading into clay (Macquaker et al., 2010; Lazar et al., 2015). It generally has a gradational top. The top sub-bed represents a clay-rich laminaset that fines upward (Macquaker et al., 2010; Lazar et al., 2015).

346 On the other hand, tempestite beds are also a product of storm waves
347 suspending sediment and inducing sediment-laden currents (Lazar et al., 2015).
348 Dominant sediment transport modes evolve from combined-flow erosion and traction
349 transport dominated by suspended load to suspension settling from waning currents
350 (Lazar et al., 2015). Tempestite beds are generally characterized by a single bed,
351 which fines upward smoothly throughout its thickness (Lazar et al., 2015). The base
352 of the tempestite bed is characterized by the presence of scouring, curved to wavy,
353 with relatively high local relief (Lazar et al., 2015). In the overall bed, laminae may be
354 broadly curved near their base to planar upwards, and basal laminasets typically lap
355 onto basal scour and fill in scour relief, whereas overlying lamina may be more poorly
356 defined and diffuse (Lazar et al., 2015).

357 In the present study, it is difficult to precisely distinguish between wave-
358 enhanced sediment-gravity flow beds or tempestite beds because it is rare that all
359 diagnostic lithofacies characteristics can be observed at once. In the case of beds b
360 and c of the sample 2013-5-5 (Fig. 3G), the characteristics are closer to tempestite
361 beds because each bed shows a gradual, consistent fining-upward motif. Regardless,
362 the presence of thin-bedded silty mudstone of either wave-enhanced sediment-gravity
363 flow or tempestite origin in the main phase of the $\delta^{13}C$ excursion clearly indicates that
364 energetic conditions associated with enhanced storm activity were prevalent during
365 the excursion interval, at least on the northwest Panthalassic margin. This
366 interpretation is consistent with the recent observations in western Tethys by Krencker
367 et al. (2015).

368

369 *5.2.3. Hyperpycnites*

370

As noted in the results section, sandstone hyperpycnites are recognised in the Sakuraguchi-dani succession for the first time (Fig. 2). Cut/polished section analysis of these sandstones reveals key features diagnostic of deposition by hyperpycnal flows. For the sandstone sample 2016-S1-m1.47 (2.6 m section height; Fig. 3H), the lithofacies can be subdivided into three parts: a = massive sandy facies, b = plant-debris-rich poorly sorted sandy facies, and c = faintly laminated silty facies with abundant plant debris (Fig. 3H). According to Yoshida et al. (2009) and Zavala et al., 2011, hyperpycnal flows commonly produce a layer of concentrated terrigenous organic matter in the uppermost part of a hyperpycnite, which is consistent with the observed lithofacies change in 2016-S1-m1.47 (Fig. 3H). This plant matter rich layer emphasises a direct connection between the extra-basinal fluvial system and the depositional environment (Zavala et al., 2011). For the sandstone sample 2016-S1-SST5 (6.4 m section height; Fig. 4), detailed observation reveals that this is a composite sandy bed. The bed is subdivided into four facies: a = massive sandy facies, b = faint, thin finer facies, c = massive sandy facies, and d = laminated silty facies (Fig. 4). These facies differences are supported by grain-size analysis (Fig. 4; Table S2 in supplementary materials). The whole lithofacies characteristics of the sample 2016-S1-SST5 are very similar to those of a specific type of hyperpycnite bed (shown in Fig. 13D in Zavala et al., 2011), which are interpreted to form by a single, long-lived hyperpycnal discharge (Zavala et al., 2011). Furthermore, in sub-facies c (massive sandy facies), a distinct grain-size change was recognised, which is characterized by coarsening upward trend followed by a fining upward trend (Fig. 4; Table S2 in supplementary materials). This grading motif is a key criterion for hyperpycnite identification (Mulder et al., 2003), and reinforces our interpretation that the sample 2016-S1-SST5 is hyperpycnite.

5.3. Enhanced hydrological cycling in response to carbon-forced warming

The temporal coincidence between the main phase of the $\delta^{13}C$ excursion and the occurrence of sedimentary features indicative of high-energy conditions and advective transport suggests a causal, climatic link (Figs. 2 and 3). In particular, the concentration of fluid-mud layers and hyperpycnites during the $\delta^{13}C$ excursion, as well as the increase in silt lamina thicknesses, suggests it was an interval of enhanced fluvial discharge. This interpretation is consistent with the postulated increase in terrestrial organic matter and detrital flux inferred from TOC/N and elemental data by Kemp and Izumi (2014). In addition, an increase in storm frequency/intensity, or at least enhanced bottom-water energy conditions, is supported by the concentration of cross laminations, erosive silt layers, silt beds, putative tempestites and wave enhanced sediment gravity flows.

The occurrence of these features within the $\delta^{13}C$ excursion could ostensibly be explained by sea-level fall (e.g. Duarte et al., 2007). However, this possibility is unlikely given the relatively deep~~er~~ water setting of the Nishinakayama Formation compared to the rest of the Toyora Group (Hirano, 1973; Kawamura, 2010), in agreement with the evidence that the Toarcian excursion took place in the context of a worldwide increase and maximum in relative sea level (Hesselbo, 2008 and references therein). Instead, our data suggest a causal link between Toarcian C release and enhanced hydrological cycling. Importantly, this is supported by data from Boreal/Tethyan locations. In Yorkshire, UK, a sudden increase in seawater temperatures inferred from O-isotope and Mg/Ca data, and enhanced global weathering inferred from Os-isotopes, are coeval with the onset of the $\delta^{13}C$ excursion

(Bailey et al., 2003; Cohen et al., 2004; Percival et al., 2016; Them et al., 2017a,b). Os-isotope evidence for increased global weathering during the Toarcian event has also recently been ~~recently~~ provided by Percival et al. (2016) and Them et al. (2017a). Similar evidence for enhanced hydrological cycling has also been determined from European and Moroccan sections by Ca-isotopes (Brazier et al., 2015) and sedimentology (Hesselbo et al., 2007; Krencker et al., 2015). Our new data from the Panthalassa Ocean margin demonstrate the global nature of this strengthening of the hydrological cycle, facilitated by carbon-forced warming and the consequent effect that this would have on atmospheric water storage and global weather systems (Trenberth, 1999; Bender et al., 2010; Krencker et al., 2015).

6. Conclusions

Our new study of one of the most expanded early Toarcian successions available reveals a rapid decrease in $\delta^{13}C$ correlable with high-resolution records obtained from European successions. Sedimentological data demonstrates a stratigraphic coincidence between rapid carbon ~~effusion~~ emission and a sudden strengthening of the hydrological cycle, which suggests that environmental responses to warming driven by rapid C release were geologically rapid. Our study helps to demonstrate how the enhancement in hydrological cycling during the Toarcian event was globally significant. This perturbation to global climate persisted throughout the main phase of the excursion characterised by minimum $\delta^{13}C$ values, an interval spanning at least 200 k.y. (Suan et al., 2008; Boulila et al., 2014).

Acknowledgements

Part of this work was financially supported by JSPS grants 24-8818 and 15J08821 to KI. DBK acknowledges recipe of NERC Fellowship NE/I02089X/1 and grants from the Sasakawa Foundation of Great Britain and Daiwa Anglo-Japanese Foundation. This study contributes to IGCP 655. We thank M. Ikeda, T. Ohta, K. Suzuki, N. Nishida and K. Kawano for assistance in the field and/or helpful discussion. Fieldwork was carried out with full permission and support from its landowners. S. Nicoara and S. Kurokawa are thanked for analytical assistance. The comments of the Editor (D. Vance) and three reviewers (G. Suan, S. Bodin, and an anonymous reviewer) greatly improved the manuscript.

Appendix A. Supplementary material

Supplementary materials (one illustration Fig. S1, and two datasheets Table S1 and Table S2) related to this article can be found online at http://dx.doi.org/XX.XXXX/j.epsl.XXXX.XX.XXX.

References

Bailey, T.R., Rosenthal, Y., McArthur, J.M., van de Schootbrugge, B., Thirlwall, M.F., 2003. Paleoceanographic changes of the Late Pliensbachian-early Toarcian interval: a possible link to the genesis of an Oceanic Anoxic Event. Earth Planet. Sci. Lett. 212, 307–320.

Behar, F., Beaumont, V., Penteado, H.L., De B., 2001. Rock-Eval 6 technology: Performance and developments. Oil Gas Sci. Tech. 56, 111–134.

Bender, M.A., Knutson, T.R., Tuleya, R.E., Sirutis, J.J., Vecchi, G.A., Garner, S.T., Held, I.M., 2010. Modeled impact of anthropogenic warming on the frequency of intense hurricanes. Science 327, 454–458.

Boulila, S., Galbrun, B., Huret, E., Hinnov, L.A., Rouget, I., Gardin, S., Bartolini, A., 2014. Astronomical calibration of the Toarcian Stage: Implications for sequence stratigraphy and the duration of the Early Toarcian OAE. Earth Planet. Sci. Lett. 386, 98–111.

Brazier, J-M., Suan, G., Tacail, T., Simon, L., Martin, J.E., Mattioli, E., Balter, V., 2015. Calcium isotope evidence for dramatic increase of continental weathering during the Toarcian oceanic anoxic event (Early Jurassic). Earth Planet. Sci. Lett. 411, 164–176.

Cohen, A.S., Coe, A.L., Harding, S.M., Schwark, L., 2004. Osmium isotope evidence for the regulation of atmospheric CO_2 by continental weathering. Geology 32, 157–160.

Dalrymple, R.W., Baker, E.K., Harris, P.T., Hughes, M.G., 2003. Sedimentology and stratigraphy of a tide-dominated, foreland-basin delta (Fly River, Papua New Guinea), in: Sidi, F.H., Nummedal, D., Imbert, P., Darman, H., Posamentier, H.W. (Eds.),

494 Tropical Deltas of Southeast Asia—Sedimentology, Stratigraphy, and Petroleum
495 Geology. SEPM Special Publication 76, pp. 147–173.
496
497 Duarte, L.V., Oliveira, L.C., Rodigues, R., 2007. Carbon isotopes as a sequence
498 stratigraphic tool: examples from the Lower and Middle Toarcian marly limestones of
499 Portugal. Bol. Geol. Min. España. 118, 3–18.
500
501 Faas, R.W., 1991. Rheological boundaries of mud: Where are the limits? Geo-Mar.
502 Lett. 11, 143–146.
503
504 Hermoso, M., Minoletti, F., Rickaby, R.E.M., Hesselbo, S.P., Baudin, F., Jenkyns,
505 H.C., 2012. Dynamics of a stepped carbon-isotope excursion: Ultra high-resolution
506 study of Early Toarcian environmental change. Earth Planet. Sci. Lett. 319–320, 45–
507 54.
508
509 Hesselbo, S.P., 2008. Sequence stratigraphy and inferred relative sea-level change
510 from the onshore British Jurassic. P. Geologists. Assoc. 119, 19–34.
511
512 Hesselbo, S.P., Pienkowski, G., 2011. Stepwise atmospheric carbon-isotope excursion
513 during the Toarcian Oceanic Anoxic Event (Early Jurassic, Polish Basin). Earth
514 Planet. Sci. Lett. 301, 365–372.
515
516 Hesselbo, S.P., Gröcke, D.R., Jenkyns, H.C., Bjerrum, C.J., Farrimond, P., Morgans
517 Bell, H.S., Green, O.R., 2000. Massive dissociation of gas hydrate during a Jurassic
518 oceanic event. Nature 406, 392–395.

519

520 Hesselbo, S.P., Morgans-Bell, H.S., McElwain, J.C., Rees, P.M., Robinson, S.A.,
521 Ross, C.E., 2003. Carbon-cycle perturbation in the Middle Jurassic and accompanying
522 changes in the terrestrial paleoenvironment. J. Geol. 111, 259–276.

523

524 Hesselbo, S.P., Jenkyns, H.C., Duarte, L.V., Oliveira, L.C.V., 2007. Carbon-isotope
525 record of the Early Jurassic (Toarcian) Oceanic Anoxic Event from fossil wood and
526 marine carbonate (Lusitanian Basin, Portugal). Earth Planet. Sci. Lett. 253, 455–470.

527

528 Hill, P.S., Fox, J.M., Crockett, J.S., Curran, K.J., Friedrichs, C.T., Geyer, W.R.,
529 Milligan, T.G., Ogston, A.S., Puig, P., Scully, M.E., Traykovski, P.A., Wheatcroft,
530 R.A., 2007. Sediment delivery to the seabed on continental margins, in: Nittrouer,
531 C.A., Austin, J.A., Field, M.E., Kravitz, J.H., Syvitski, J.P.M., Wiberg, P.L. (Eds.),
532 Continental Margin Sedimentation: From Sediment Transport to Sequence
533 Stratigraphy. International Association of Sedimentologists Special Publication 37, pp.
534 49–99.

535

536 Hirano, H., 1973. Biostratigraphic study of the Jurassic Toyora Group, part 3. Trans.
537 Proc. Palaeont. Soc. Japan, N.S. 90, 45–71.

538

539 Ichaso, A.A., Dalrymple, R.W., 2009. Tide- and wave-generated fluid mud deposits in
540 the Tilje Formation (Jurassic), offshore Norway. Geology 37, 539–542.

541

542 Izumi, K., Miyaji, T., Tanabe, K., 2012. Early Toarcian (Early Jurassic) oceanic
543 anoxic event recorded in the shelf deposits in the northwestern Panthalassa: evidence

544 from the Nishinakayama Formation in the Toyora area, west Japan. Palaeogeogr.
545 Palaeoclimatol. Palaeoecol. 315–316, 100–108.
546
547 Izumi, K., Suzuki, R., Inui, M., 2017. Estimating the degree of mudstone
548 compactional thinning: Empirical relationship between mudstone compaction and
549 geochemical composition. Trans. Kokushikan Univ. Sci. Eng., Tokyo, Japan 10, 29–
550 37.
551
552 Jenkyns, H.C., Gröcke, D.R., Hesselbo, S.P., 2001. Nitrogen isotope evidence for
553 water mass denitrification during the early Toarcian (Jurassic) oceanic anoxic event.
554 Palaeoceanography 16, 593–603.
555
556 Kawamura, H., 2010. Stratigraphic revision of the Jurassic Toyora Group of the
557 southern part of the Tabe Basin, Yamaguchi Prefecture, southwest Japan. Jour. Geol.
558 Soc. Japan 116, 27–44. (in Japanese with English abstract)
559
560 Kemp, D.B., Izumi, K., 2014. Multiproxy geochemical analysis of a Panthalassic
561 margin record of the early Toarcian oceanic anoxic event (Toyora area, Japan).
562 Palaeogeogr. Palaeoclimatol. Palaeoecol. 414, 332–341.
563
564 Kemp, D.B., Coe, A.L., Cohen, A.S., Schwark, L., 2005. Astronomical pacing of
565 methane release in the Early Jurassic period. Nature 437, 396–399.
566

567 Kemp, D.B., Coe, A.L., Cohen, A.S., Weedon, G.P. 2011. Astronomical forcing and
568 chronology of the Early Toarcian (Early Jurassic) Oceanic Anoxic Event in
569 Yorkshire, UK. Paleoceanography 26, PA4210.
570
571 Krencker, F-N., Bodin, S., Suan, G., Heimhofer, U., Kabiri, L., Immenhauser, A.,
572 2015. Toarcian extreme warmth led to tropical cyclone intensification. Earth Planet.
573 Sci. Lett. 425, 120–130.
574
575 Lazar, O.P., Bohacs, K.M., Schieber, J., Macquaker, J.H.S., Demko, T.M., 2015.
576 Mudstone Primer: Lithofacies variations, diagnostic criteria, and sedimentologic-
577 stratigraphic implications at lamina to bedset scales. SEPM Concepts in
578 Sedimentology and Paleontology 12, 198 p.
579
580 Macquaker, J.H.S., Bentley, S.J., Bohacs, K., Lazar, R., Jonk, R., 2010. Wave-
581 enhanced sediment-gravity flows and mud dispersal across continental shelves:
582 Reappraising sediment transport processes operating in ancient mudstone successions.
583 Geology 38, 947–950.
584
585 McElwain, J.C., Wade-Murphy, J., Hesselbo, S.P., 2005. Changes in carbon dioxide
586 during an oceanic anoxic event linked to intrusion into Gondwana coals. Nature 435,
587 479–482.
588
589 Mulder, T., Alexander, J., 2001. The physical character of subaqueous sedimentary
590 density flows and their deposits. Sedimentology 48, 269–299.
591

592 Mulder, T., Migeon, S., Savoye, B., Faugeres, J.-C., 2001. Inversely graded turbidite
593 sequences in the deep Mediterranean. A record of deposits from flood-generated
594 turbidity currents? Geo-Mar. Lett. 21, 86–93.
595
596 Mulder, T., Syvitski, J.P.M., Migeon, S., Faugeres, J.-C., Savoye, B., 2003. Marine
597 hyperpycnal flows: initiation, behavior and related deposits. A review. Mar. Petrol.
598 Geol. 20, 861–882.
599
600 Nakada, K., Matsuoka, A., 2011. International correlation of the
601 Pliensbachian/Toarcian (Lower Jurassic) ammonoid biostratigraphy of the
602 Nishinakayama Formation in the Toyora Group, southwest Japan. Newsl. Stratigr. 44,
603 89–111.
604
605 Nishida, N., Ito, M., 2009. Fluid mud: Distinctive features and implications for
606 genetic stratigraphy. Jour. Geol. Soc. Japan 115, 149–167 (in Japanese with English
607 abstract).
608
609 Nishida, N., Ito, M., Inoue, A., Takizawa, S., 2013. Clay fabric of fluid-mud deposits
610 from laboratory and field observations: Potential application to the stratigraphic
611 record. Mar. Geol. 337, 1–8.
612
613 Percival, L.M.E., Cohen, A.S., Davies, M.K., Hesselbo, S.P., Jenkyns, H.C., Leng,
614 M.J., Mather, T.A., Storm, M.S., Xu, W. 2016. Osmium isotope evidence for two
615 pulses of increased continental weathering linked to Early Jurassic volcanism and
616 climate change. Geology 44, 759–762.

Röhl, H.-J., Schmid-Röhl, A., 2005. Lower Toarcian (Upper Liassic) black shales of the Central European Epicontinental Basin: A sequence stratigraphic case study from the SW German Posidonia Shale. SEPM Spec. Publ. 82, 165–189.

Ruebsam, W, Münzberger, P., Schwark, L., 2014. Chronology of the Early Toarcian environmental crisis in the Lorraine Sub-Basin (NE Paris Basin). Earth Planet. Sci. Lett. 404, 273–282.

Suan, G., Pittet, B., Bour, I., Mattioli, E., Duarte, L.V., Mailliot, S., 2008. Duration of the Early Toarcian carbon isotope excursion deduced from spectral analysis: consequence for its possible causes. Earth Planet. Sci. Lett. 267, 666–679.

Suan, G., van de Schootbrugge, B., Adatte, T., Fiebig, J., Oschmann, W., 2015. Calibrating the magnitude of the Toarcian carbon cycle perturbation. Paleoceanography 30, 495–509.

Svensen, H., Planke, S., Chevallier, L., Malthe-Sorenssen, A., Corfu, F., Jamtveit, B., 2007. Hydrothermal venting of greenhouse gases triggering Early Jurassic global warming. Earth Planet. Sci. Lett. 256, 554–566.

Tanabe, K., Inazumi, A., Ohtsuka, Y., Katsuta, T., Tamahama, K., 1982. Litho- and biofacies and chemical composition of the Lower Jurassic Nishinakayama Formation (Toyora Group) in west Japan. Ehime Univ. Mem. Sci. Ser. D 9, 47–62. (in Japanese with English abstract)

Them, T.R., Gill, B.C., Selby, D., Gröcke, D.R., Friedman, R.M., Owens, J.D., 2017a. Evidence for rapid weathering response to climatic warming during the Toarcian Oceanic Anoxic Event. Sci. Rep. 7, 5003.

Them, T.R., Gill, B.C., Caruthers, A.H., Gröcke, D.R., Tulsky, E.T., Martindale, R.C., Poulton, T.P., Smith, P.L., 2017b. High-resolution carbon isotope records of the Toarcian Oceanic Anoxic Event (Early Jurassic) from North America and implications for the global drivers of the Toarcian carbon cycle. Earth Planet. Sci. Lett. 459, 118–126.

Trenberth, K., 1999. Conceptual framework for changes of extremes of the hydrologic cycle with climate change. Climatic Change 42, 327–339.

Tyson, R.V., 1995. Bulk Geochemical Characterization and Classification of Organic Matter: Elemental Analysis and Pyrolysis, in: Sedimentary Organic Matter: Organic facies and palynofacies. Springer Netherlands, Dordrecht, pp. 367–382.

Wells, J.T., 1995. Tide-dominated estuaries and tidal rivers, in: Perillo, G.M.E. (Ed.), Geomorphology and Sedimentology of Estuaries. Elsevier, Amsterdam, pp. 179–205.

Yoshida, K., Kawakami, G., Kawamura, M., 1995. Heavy mineral-concentrated sandstones in the Upper Permian and the Lower Triassic of the South Kitakami Terrane. Jour. Geol. Soc. Japan 101, 279–294. (in Japanese with English abstract)

Yoshida, M., Yoshiuchi, Y., Hoyanagi, K., 2009. Occurrence conditions of hyperpycnal flows, and their significance for organic-matter sedimentation in a Holocene estuary, Niigata Plain, Central Japan. Isl. Arc 18, 320–332.

Zavala, C., Arcuri, M., Meglio, M. Di, Gamero Diaz, H., Contreras, C., 2011. A genetic facies tract for the analysis of sustained hyperpycnal flow deposits, in: Slatt, R. M., Zavala, C. (Eds.), Sediment transfer from shelf to deep water—Revisiting the delivery system. AAPG Studies in Geology 61, pp. 31–51.

Figure captions

Figure 1 | Palaeogeography of the Early Jurassic and locations of Early Toarcian deposits. Note the European bias in study locations. Inset, location map of the Sakuraguchi-dani stream valley succession in Yamaguchi Prefecture, Japan. Sakuraguchi-dani location map and palaeogeographic reconstruction redrawn from Cohen et al. (2004) and Kemp and Izumi (2014).

Figure 2 | Sedimentary log with $\delta^{13}C$ and sedimentological data through the Sakuraguchi-dani succession. Organic $\delta^{13}C$ data for bulk mudstone and wood are shown. These data delineate a ~30 m thick ~~~3‰~~ negative excursion in $\delta^{13}C$ ~~excursion~~ of ~3‰ divided into a main phase (blue shading) and recovery interval (purple shading). Mudstone $\delta^{13}C$ data below ~5 m and above ~0 m are from Kemp and Izumi (2014; see Table S1 in supplementary materials for full data listing). The onset of the shift to minimum $\delta^{13}C$ values is stepped, comprising two separate abrupt shifts (labeled A and B). Shift A straddles an inferred fault (brecciated interval; see text for

692 details). Occurrences of sedimentary features indicative of high-energy/advective
693 transport are concentrated in the main phase. Silt laminae are generally thicker during
694 the main phase. Ammonite zones are from Nakada and Matsuoka (2011).
695
696 **Figure 3** | Images of key sedimentary features in silty mudstones facies. All images
697 taken perpendicular to bedding planes. (A) Thin-section photomicrograph of parallel-
698 laminated silty mudstone (-13.62 m section height), suggesting a quiescent and likely
699 dysoxic environment. (B) Thin-section photomicrograph of bioturbated silty
700 mudstone (-12.72 m). Note the presence of *Phycosiphon* (arrows). (C) Thin-section
701 scan image of ripple cross-laminated silty mudstone (8.90 m). (D) Thin-section scan
702 image of silty mudstone showing presence of homogeneous muddy layer (-2.00 m).
703 (E) Magnified thin-section photomicrograph of homogenous muddy layer in D. This
704 layer is characterized by sharp layer contacts, absence of internal lamination, rare
705 bioturbation, and randomly scattered amorphous organic matter. This layer is
706 interpreted as a compacted fluid-mud deposit layer (see main text). (F) Thin-section
707 scan image of silty mudstones showing the presence of two (nearly amalgamated) silt
708 beds likely indicative of traction transport (2.10 m). Note that faint internal laminae
709 are recognised within these silt beds. (G) Thin-section scan image of thin-bedded silty
710 mudstone (1.00 m). At least three independent beds are recognised: a = homogeneous
711 muddy bed, which may be interpreted as a fluid-mud deposit layer, b and c = silty
712 beds with basal internal laminae showing gradual lithological change (fining upward
713 trend), which may be interpreted as storm-associated tempestites or wave-enhanced-
714 sediment-gravity-flows (see also supplementary materials). (H) Scan image of cut
715 surface of sandstone bed (2.6 m), which is subdivided into three facies: a = massive
716 sandy facies, b = plant-debris-rich poorly sorted sandy facies, and c = faintly

717 laminated silty facies with abundant plant debris. This sandstone is interpreted as a
718 hyperpycnite (see also supplementary materials). (I) Scan image of cut surface of
719 sandstone bed interpreted as a debrite (6.10 m). Note the presence of randomly
720 scattered mud clasts (arrows).
721
722 **Figure 4** | Scan image of the sandstone sample (2016-S1-SST5; 6.4 m), with graph
723 showing the internal grain-size variations and representative thin-section
724 photomicrographs of each horizon. This sample is subdivided into four lithofacies (a
725 to d in the left photograph; see text for detail). Note the characteristic grain-size
726 variation, suggesting that this bed was formed by a hyperpycnal flow (see main text
727 for details).
728
729 **Figure 5 |** Correlation of Sakuraguchi-dani and European $\delta^{13}C$ records. Records are
730 plotted on the same relative stratigraphic thickness and excursion magnitude scale
731 (shift B = 0 m). This plot helps to highlight the ~~high~~ great relative thickness of the
732 Sakuraguchi-dani $\delta^{13}C$ profile relative to European $\delta^{13}C$ profiles. Data are correlated
733 based on the presence of at least 2 stratigraphically abrupt $\delta^{13}C$ shifts in all the
734 successions (green and purple dashed lines). In some records, and in
735 the accompanying publications, a 3rd shift has also been noted/suggested (blue dashed
736 line). Evidence for a 3rd shift in the Sakuraguchi-dani record is somewhat equivocal,
737 though the general morphology of the $\delta^{13}C$ record is very similar to that recorded in
738 Portugal (Peniche section). Correlation between the UK (Yorkshire section) $\delta^{13}C$
739 profile and the Portuguese profile is based on Kemp et al. (2011). Correlation of the
740 Polish $\delta^{13}C$ (Brody-Lubienia section) terrestrial phytoclast record with the UK profile
741 is based on Hesselbo and Pienkowski (2011). Italian $\delta^{13}C$ inorganic and organic $\delta^{13}C$

742 data are from the Belluno Trough section. The German $\delta^{13}C$ profile is from the
743 Denkingen borehole. ~~French~~ Inorganic and organic $\delta^{13}C$ data in the French profile are
744 from the Sancerre borehole (all references are on figure). The termination of
745 the excursion in each record is shown by the red dashed line.

Highlights

- New high-resolution C-isotope stratigraphy from NW Panthalassa section through T-OAE.
- Rapid (i.e. millennial-scale) carbon release suggested by C-isotope data.
- Sudden strengthening of hydrological cycling in response to rapid C release.

Sedimentary evidence for enhanced hydrological cycling in response to rapid carbon release during the early Toarcian oceanic anoxic event

Kentaro Izumi[a, *], David B. Kemp[b], Shoma Itamiya[c], and Mutsuko Inui[c]

[a]*Faculty & Graduate School of Education, Chiba University, 1-33 Yayoi-cho, Inage-ku, Chiba-shi, Chiba 263-8522, Japan*

[b]*School of Geosciences, University of Aberdeen, Old Aberdeen, Aberdeen, AB24 3UE, UK*

[c]*School of Science and Engineering, Kokushikan University, 4-28-1 Setagaya, Setagaya-ku, Tokyo 154-8515, Japan*

*Corresponding author at: Faculty & Graduate School of Education, Chiba University, Chiba, Japan.

E-mail address: izumi@chiba-u.jp (K. Izumi).

ABSTRACT

A pronounced excursion in the carbon-isotope composition of biospheric carbon and coeval seawater warming during the early Toarcian (~183 Ma) has been linked to the large-scale transfer of ^{12}C-enriched carbon to the oceans and atmosphere. A European bias in the distribution of available data means that the precise pattern, tempo and global expression of this carbon cycle perturbation, and the associated environmental responses, remain uncertain. Here, we present a new cm-scale

terrestrial-dominated carbon-isotope record through an expanded early Toarcian section from Japan that displays a negative excursion pattern similar to marine and terrestrial carbon-isotope records documented from Europe. These new data suggest that ^{12}C-enriched carbon was added to the biosphere in at least one rapid, millennial-scale pulse. Sedimentological analysis indicates a close association between the carbon-isotope excursion and high-energy sediment transport and enhanced fluvial discharge. Together, these data support the hypothesis that a sudden strengthening of the global hydrological cycle occurred in direct and immediate response to rapid carbon release and atmospheric warming.

Keywords: Toarcian, carbon isotope, hydrological cycling, sedimentology, atmospheric warming

1. Introduction

The widespread occurrence of organic-rich facies deposited under reducing conditions during the early Toarcian has led to the recognition of one of the most pronounced oceanic anoxic events (OAEs) of the Phanerozoic. Broadly contemporaneous with deoxygenation is evidence for abrupt warming (Bailey et al., 2003), an increase in continental chemical weathering rates (Brazier et al., 2015; Cohen et al., 2004; Percival et al., 2016; Them et al., 2017a), and changes in atmospheric pCO_2 (McElwain et al., 2005). The major sedimentary reservoirs of carbon at this time record a 3-7‰ negative excursion in carbon-isotopes ($\delta^{13}C$), indicative of a large input of ^{12}C-enriched carbon (Hesselbo et al., 2000; Kemp et al., 2005; Svensen et al., 2007). Carbon-isotope records from Boreal and Tethyan sections

often show that the overall shift to minimum values was stepped, comprising at least two rapid negative shifts in $\delta^{13}C$ superimposed on a more protracted decrease (e.g. Bodin et al., 2016; Hermoso et al., 2009; Hesselbo and Pienkowski, 2011; Jenkyns et al., 2001; Kemp et al., 2005; Ruebsam et al., 2004; Suan et al., 2015).

This $\delta^{13}C$ morphology has not yet been convincingly replicated outside of the Boreal and Tethyan realms, although recent work by Them et al. (2017b) indicates evidence for a complex and possibly stepped structure to the onset of the excursion in North America (Eastern Panthalassa Ocean). Establishing the precise pattern, reproducibility and magnitude of the early Toarcian $\delta^{13}C$ excursion is of central importance for determining the ultimate cause(s) of the event and associated environmental change. Similarly, there is a lack of data elucidating the environmental responses to inferred carbon release from globally distributed settings. These issues limit our understanding of the effects (both local and global) of carbon-forced greenhouse warming, and hence the role that events like the early Toarcian can play as analogues for modern day C release scenarios. To address these issues, we have conducted a high-resolution organic carbon-isotope and sedimentological analysis of an expanded early Toarcian succession from Japan that was deposited at the margin of the Panthalassa Ocean (Fig. 1).

2. Geological setting

Lower Toarcian organic-rich mudstones, siltstones and fine-grained sandstones of the Nishinakayama Formation (Toyora Group) crop out in the Toyora area of southwest Japan, Yamaguchi prefecture (Fig. 1). The rocks form part of the fill of the Tabe Basin. A long history of research on the Sakuraguchi-dani stream bed

74 succession (131° 03'E 34° 08'E; Fig. 1) has revealed a rich ammonite fauna, allowing
75 demarcation of the lower Toarcian (Nakada and Matsuoka, 2011 and references
76 therein). Recent geochemical analysis of the succession has demonstrated that the
77 early Toarcian carbon cycle perturbation is well expressed, with a ~3‰ negative
78 excursion recorded in organic carbon-isotopes spanning ~30 m (Izumi et al., 2012;
79 Kemp and Izumi, 2014).
80
81 **3. Analytical methods**
82
83 *3.1. Carbon isotope analysis*
84
85 For this study, 80 mudstone samples were collected, primarily across the ~5 m
86 interval comprising the onset of the excursion, and analysed for the $\delta^{13}C$ of organic
87 carbon. In addition, $\delta^{13}C$ analysis was also carried out on 6 macrofossil wood
88 samples. For mudstone and wood $\delta^{13}C$ measurements, powdered samples were
89 decalcified in 3M HCl (heated to 60°C for 3 hours in the case of wood samples to
90 help remove pyrite) and then washed with deionised water until neutrality was
91 reached. After drying, samples were weighed into tin capsules and analysed on a
92 Europa Scientific 20/20 mass spectrometer (rock samples) or a Thermo Scientific
93 MAT253 isotope ratio mass spectrometer (wood samples). Precision for both
94 instruments was quantified via analysis of standards, and was better than 0.2‰.
95
96 *3.2. Rock-Eval analysis*
97

Organic matter was characterised by Rock-Eval pyrolysis of 5 mudstone samples. Rock-Eval pyrolysis was carried out on 5 powdered samples distributed through the succession using a Rock-Eval 6 apparatus (Vinci Technologies), run in 'Basic Method' mode (see Behar et al., 2001). Both the S1 and S2 signals were successively determined with flame ionization detection. The S1 signal corresponds to the amount of free hydrocarbons volatilized for 3 min at 300 °C, and the S2 signal represents the amount of hydrocarbons generated from kerogen cracking between 300 and 650 °C with a heating rate of 25 °C per 1 min. The amount of CO_2 generated between 300 and 400 °C was determined as the S3 signal, with infrared detection. All parameters (S1, S2, and S3) are expressed in mg of hydrocarbons or CO_2 per gram of rock. T_{max} is the temperature at which the maximum hydrocarbon yield resulting from kerogen cracking occurs. Residual organic carbon contents of the pyrolyzed samples were obtained by combustion in air from 300 to 650 °C, with a heating rate of 20 °C per 1 min. The CO_2 and CO resulting from this combustion was also determined with an infrared cell, and corresponds to peak S4CO_2 for CO_2 and peak S4CO for CO. By using these parameters with the S1 to S3 signals, the total organic carbon (TOC) content (wt.%) was calculated as the sum of pyrolyzed and residual organic carbon. The hydrogen index (HI, mg HC/g TOC) and oxygen index (OI, mg CO_2/g TOC) were calculated as S2/TOC, and S3/TOC, respectively.

For the application of Rock-Eval pyrolysis to the Toarcian sediments with basic interpretations, see Röhl and Schmid-Röhl (2005) for instance.

3.3. Sedimentological analysis

The sedimentology of the entire succession was investigated based on thin-section study of 72 mudstone samples, and polished/cut surface study of 28 sandstone samples. All thin-section observations were carried out using a polarizing microscope (BX-51, Olympus) at Kokushikan University. In this study, silt beds are defined as silty layers with internal silty laminae, whereas a silt lamina is the smallest macroscopic layer without internal layering. Silt lamina thicknesses were measured from thin-section scanned images (jpeg format), using ImageJ image-processing software. Thin-section scanned images were obtained using a film scanner (KFS-1400, Kenko film scanner) that is equipped with polarizers. For thickness measurement of individual silt laminae, only distinct and continuous silt laminae recognised in a scan image were used. In the case of silt lamina whose thickness changes horizontally, the maximum thickness was used. All individual thickness data obtained from the single thin-section scanned image were used when calculating average thickness. Measurements of silt bed thicknesses were carried out in the same way.

For sandstone sedimentological analysis, sandstone samples were cut perpendicular to bedding planes and polished if necessary. Such cut or polished surfaces were scanned using a flatbed image scanner (GT-X770, EPSON). For one sandstone sample (Sample ID: 2016-S1-SST5), grain-size analysis was conducted in order to investigate the detailed sedimentary features that are difficult to identify by naked-eye observation. Grain-size analysis was based on the method described in Yoshida et al. (1995), which performs measurements of long-axis diameters of monocrystalline quartz grains under thin-section observation. In this study, long-axis diameters of monocrystalline quartz grains were measured in ImageJ using 5 x 5 mm meshed jpeg images of thin-section photomicrographs.

4. Results

4.1. Carbon-isotope data and Rock Eval analysis

Our cm-scale $\delta^{13}C$ analysis of mudstones across the interval comprising the onset of the excursion reveals a steady decrease of ~0.7‰ over the lowermost ~13 m of the succession, from ~-24.8‰ to ~-25.5‰ (Fig. 2). At -4.58 m in the section, a -2.3‰ shift in $\delta^{13}C$ occurs over 21 cm of strata (labelled A on Fig. 2; Table S1 in supplementary materials). This decrease straddles an 18 cm thick horizon of unconsolidated, poorly sorted (clay to pebble sized) mudstone fragments. This is interpreted as a fault breccia (Fig. 2), though the lateral extent of the outcrop (~20 cm) and position within a stream bed prevents a fuller assessment. Ammonite biostratigraphy indicates an early Toarcian age for strata immediately below and above this inferred fault (*P. paltus* Zone, Fig. 2). Above this decrease, $\delta^{13}C$ increases by ~1‰ over the succeeding ~2 m (Fig. 2). Between -2.59 and -2.33 m, there is a second, broadly defined decrease in $\delta^{13}C$ of -2.2‰ (Fig. 2). This second decrease is interrupted by a positive excursion of ~2.3‰ that occurs over 6 cm, from -2.44 to -2.38 m (Fig. 2). Between -2.38 and -2.33 m, there is a very abrupt negative shift in $\delta^{13}C_{organic}$ of -2.9‰ (labelled B on Fig. 2; Table S1 in supplementary materials). Macrofossil wood $\delta^{13}C$ data broadly track bulk mudstone $\delta^{13}C$ (Fig. 2; Table S1 in Appendix A). Our Rock-Eval results indicate extremely low hydrogen index (i.e. 1 to 3) and oxygen index (i.e. 5 to 23) values (Figure S1 in supplementary material). These data suggest that the organic matter is predominantly Type IV kerogen. It is widely recognized that Type IV kerogen generally consists of oxidised intertinite of higher

plant origin, although it may also consist of oxically degraded, plankton derived, fine-grained, amorphous material (Tyson, 1995). The abundant presence of both macro- and microscopic fossil wood and plant debris (Kemp and Izumi, 2014) suggests that the organic matter in the studied mudstones is indeed dominated by oxidised intertinite of higher plant origin.

4.2. Mudstone sedimentology

Three primary mudstone lithofacies can be identified in the succession: 1) laminated (ranging from well laminated to poorly laminated), 2) bioturbated, and 3) thin-bedded (Fig. 3). Parallel lamination, indicating quiescent and likely oxygen-deficient conditions, is recognised in mudstones throughout the studied interval (see also Izumi et al., 2012). However, our detailed microscopic thin-section analysis also reveals the presence of sedimentary features indicative of advective transport and oxygenated, high-energy conditions. Notably, we recognise cross laminations, irregular silty layers (e.g. wavy or lenticular silt laminae, often with erosional bases), silt beds, fluid-mud layers, putative tempestites/wave enhanced sediment gravity flow deposits, and burrows (Figs. 2 and 3; see also Table S2 in supplementary materials). Among these sedimentary features, fluid-mud layers and putative tempestites/wave enhanced sediment gravity flow deposits are described from the Nishinakayama Formation for the first time. Burrows (e.g. *Phycosiphon*) were recognised throughout the succession (Fig. 2). Crucially, however, sedimentary features indicative of high-energy conditions are concentrated between -4.53 and ~14 m, broadly coincident with the main phase of the $\delta^{13}C$ excursion (Fig. 2).

196 The thicknesses of silt laminae measured in thin sections of the mudstone
197 facies vary through the studied interval (from 0.08 to 0.849 mm, mean 0.26 mm; see
198 also Table S2 in supplementary materials). Between -16.02 and -4.53 m, silt laminae
199 are of broadly consistent thickness (~0.2 mm). At -4.46 m, and coincident with the
200 onset of the $\delta^{13}C$ excursion, silt laminae thicknesses increase and show greater
201 variability (Fig. 2). Thicknesses remain highly variable through the main phase of the
202 $\delta^{13}C$ excursion between -4.46 m and ~10 m. Average thickness and variability
203 decreases between ~10 m and ~25 m, coeval with decreasing $\delta^{13}C$ (Fig. 2). Laminae
204 thicknesses are broadly stable between ~25 m and 50 m (Fig. 2).
205
206 *4.3. Sandstone sedimentology*
207
208 Sandstone beds are concentrated between ~0 and ~7 m within the main phase
209 of the $\delta^{13}C$ excursion (Fig. 2), and have previously been interpreted as turbidites
210 (Kawamura, 2010). Based on detailed observation of sandstone cut and polished
211 surfaces of 28 samples, however, three types of sediment gravity flow deposits were
212 identified: turbidites (16 samples), debrites (9 samples), and hyperpycnites (3
213 samples). Most notably, debrites (Fig. 3I) and hyperpycnites (Figs. 3H and 4) are
214 described from the Nishinakayama Formation for the first time. The recognition of
215 hyperpycnites, which are formed by hyperpycnal flows generated by river floods
216 (Mulder and Alexander, 2001; Mulder et al., 2001, 2003), is especially important for
217 palaeoclimatic interpretations as discussed below (see section 5.2).
218
219 **5. Discussion**
220

221 *5.1. Evidence for rapid carbon release during the Early Toarcian*

222

223 Rock-Eval data (Fig. S1), coupled with the similarity between the mudstone
224 and macrofossil wood $\delta^{13}C$ data (Fig. 2), emphasizes the dominantly terrestrial nature
225 of the organic matter in the Sakuraguchi-dani succession (see also Kemp and Izumi,
226 2014). Hence, the bulk mudstone $\delta^{13}C$ data in the succession predominantly reflect
227 the composition of CO_2 in the early Toarcian atmosphere. Two negative shifts are
228 present across the onset of the $\delta^{13}C$ excursion in the succession (labeled A and B, -
229 2.3‰ and -2.9‰ respectively, Fig. 2). The magnitude of these shifts is comparable to
230 the magnitude of similar and correlable shifts recognised in marine and terrestrial
231 organic matter from European successions (~1-4‰, see also Fig. 5). The veracity of
232 shift A cannot be ascertained, and its brevity is almost certainly a consequence of the
233 inferred fault. Nevertheless, $\delta^{13}C$ values immediately below and above the inferred
234 fault-related brecciated interval at shift A show increasing trends (Fig. 2), and thus a
235 negative shift of uncertain brevity (though spanning less than one ammonite Zone)
236 must have occurred between deposition of the strata preserved below and above the
237 inferred fault.

238 There is no sedimentological evidence for a fault or break in sedimentation
239 across the larger, second negative $\delta^{13}C$ shift beginning at -2.38 m (shift B, Fig. 2).
240 This shift corresponds to <0.15% of the sandstone-free thickness of the overall
241 excursion (~5 cm versus ~34 m). Considering a timescale of ~500-900 k.y. for the
242 excursion as a whole (Boulila et al., 2014; Suan et al., 2008), and notwithstanding
243 mixing/residence time constraints on the expression of $\delta^{13}C$ changes and
244 sedimentation rate variations, shift B likely has a millennial-scale duration (~0.7-1.3
245 k.y.). This is consistent with Kemp et al. (2005), who described similarly

stratigraphically abrupt shifts in $\delta^{13}C$ from Yorkshire, UK. Although rapid $\delta^{13}C$ changes in the early Toarcian very likely occurred within the context of more protracted C emission and warming from volcanic CO_2 sources (e.g. Kemp et al., 2005; Svensen et al., 2007; Suan et al., 2008), our findings emphasise the global nature and rapidity of these changes. Our data thus implicitly support a rapid, global C release mechanism such as hydrate dissociation (e.g. Hesselbo et al., 2000; Kemp et al., 2005).

5.2. Sedimentary features indicative of enhanced fluvial discharge and energetic bottom conditions: identification and palaeoclimatic implications

5.2.1. Fluid-mud deposit layers

Thin-section analysis of silty mudstones reveals the presence of distinct thin (~mm scale) muddy layers, whose lithofacies differ from that of surrounding silty mudstones with parallel-laminated lithofacies (Fig. 3A). The general lithofacies of these distinct thin muddy layers is characterized by: 1) homogeneous internal structure with no or very rare presence of faint laminations, 2) sharp bed contacts, 3) lack of bioturbation, and 4) relatively finer-grained composition with randomly scattered amorphous organic debris (Fig. 3D, E). The lithofacies of these thin muddy layers match those described previously in fluid-mud deposits (Dalrymple et al., 2003).

A fluid mud is defined as a high-density, bottom-hugging mobile subaqueous body of fine-grained suspended-sediment with a concentration of > 10g/L (Faas, 1991). Fluid mud is composed primarily of clay- to silt-sized particles with variable

amounts of organic matter (Dalrymple et al., 2003). On the basis of recent experiments and observations, fluid-mud deposits are characterized by: 1) homogeneous and structureless muddy layers (e.g. lack of internal laminations and grading), 2) sharp basal contacts, 3) rare bioturbation, 4) aggregates of clay particles in face-to-face contact with each other (FF-aggregates), and 5) initial thickness of > ~1 cm (Dalrymple et al., 2003; Nishida et al., 2013). Among these characteristics, FF aggregates can be destroyed by sediment diagenesis and thus may not be recognized in lithified strata, although they are preserved in historical layers in modern core samples and young (i.e. Quaternary) records (Nishida and Ito, 2009; Nishida et al., 2013).

With respect to thickness of fluid-mud deposits, it is generally considered that >~1 cm (>~5 mm after compaction) is a minimum thickness to distinguish fluid-mud layers from other muddy layers that accumulated by slow, particle-by-particle settling from suspension (Ichaso and Dalrymple, 2009). Although distinct muddy layers recognized within the silty mudstones of the Nishinakayama Formation are very similar to fluid-mud deposits, in most cases their thicknesses are <5 mm. Nevertheless, estimation of the minimum thickness of fluid-mud deposit layers in ancient strata by Ichaso and Dalrymple (2009) was not supported by data. According to a recent study estimating the degree of mudstone compactional thinning (Izumi et al., 2017), mudstones with low Ca abundances are generally affected more by mechanical compaction than Ca-rich mudstones. Mudstones of the Nishinakayama Formation have very low Ca abundances (0.21 to 5.99 wt.% as CaO; Tanabe et al., 1982), and therefore may have been greatly affected by mechanical compaction, resulting in >~70 % thinning according to the empirical relationship between the degree of mudstone compactional thinning and CaO abundances (Izumi et al., 2017).

It is also important to emphasize that the empirical relationship of Izumi et al. (2017) has a lwide 95% confidence interval, and that the degree of compactional thinning of the muddy layers from the Nishinakayama Formation might have reached >~90 % (upper limit of 95% confident interval).

Based on the considerations above, we suggest that the distinct muddy layers from the Nishinakayama Formation are compacted fluid-mud deposit layers. Because the Nishinakayama Formation represents fully marine conditions (Tanabe et al., 1982), the inferred fluid-mud deposits were likely formed by either 1) intense wave action generated by storms, or 2) by increased sediment supply due to flood events (Hill et al., 2007; Ichaso and Dalrymple, 2009). Although it is difficult to precisely distinguish these two possibilities, the latter may be more likely in the case of the Nishinakayama Formation because no large-scale hummocky cross stratification has been recognized (Kawamura, 2010). Nevertheless, as discussed below (section 5.2.2), sedimentary features of probable storm origin are also recognized from the studied section, and thus at least some proportion of the fluid-mud deposits we recognise could have a storm-related origin.

5.2.2. Putative tempestites/wave enhanced sediment gravity flow deposits

Parallel lamination in mudstones is generally interpreted to indicate continuous sediment accumulation by suspension settling under relatively still and oxygen-depleted bottom environments (Lazar et al., 2015). However, thin-bedded mudstones are normally formed as a result of discontinuous sediment accumulation by lateral transport in bed load, for instance under intermittently energetic conditions (Lazar et al., 2015). Based on our observation, thin-bedded silty mudstones only occur

between -2.38 to 3.5 m, which corresponds with the middle part of the 'main phase' of the $\delta^{13}C$ excursion (Fig. 2). This suggests that relatively energetic conditions were dominant during the main phase of the $\delta^{13}C$ excursion. Fig. 3G shows an example of a thin-bedded silty mudstone (Sample ID: 2013-5-5). In this case, at least three independent beds can be recognized: a = homogeneous muddy bed, and b & c = silty beds with basal internal laminae showing gradual lithological change (fining upward trend) (Fig. 3G). Bed a is interpreted as fluid-mud deposit layer due to its homogeneous lithofacies, finer-grained (muddy) composition, rare bioturbation structures, and sharp bed boundary. Beds b and c are very similar to wave-enhanced sediment-gravity flow produced beds or tempestite beds (Macquaker et al., 2010). Wave-enhanced sediment-gravity flow beds are a likely product of storm-induced waves, and are generally subdivided into three sub-beds; namely, the basal, middle, and top sub-beds produced by traction transport, sediment-gravity flow, and suspension settling, respectively (Macquaker et al., 2010; Lazar et al., 2015). From the lithofacies point of view, the basal sub-bed represents a laminaset composed of silt-rich and largely homogeneous to slightly graded material (Macquaker et al., 2010; Lazar et al., 2015). The basal sub-bed may not be continuous in some cases, and it has a sharp to gradational top. The basal sub-bed indicates traction transport. The middle sub-bed also represents a laminaset composed of multiple, very thin broadly curved to wavy laminae composed of silt grading into clay (Macquaker et al., 2010; Lazar et al., 2015). It generally has a gradational top. The top sub-bed represents a clay-rich laminaset that fines upward (Macquaker et al., 2010; Lazar et al., 2015).

On the other hand, tempestite beds are also a product of storm waves suspending sediment and inducing sediment-laden currents (Lazar et al., 2015). Dominant sediment transport modes evolve from combined-flow erosion and traction

transport dominated by suspended load to suspension settling from waning currents (Lazar et al., 2015). Tempestite beds are generally characterized by a single bed, which fines upward smoothly throughout its thickness (Lazar et al., 2015). The base of the tempestite bed is characterized by the presence of scouring, curved to wavy, with relatively high local relief (Lazar et al., 2015). In the overall bed, laminae may be broadly curved near their base to planar upwards, and basal laminasets typically lap onto basal scour and fill in scour relief, whereas overlying lamina may be more poorly defined and diffuse (Lazar et al., 2015).

In the present study, it is difficult to precisely distinguish between wave-enhanced sediment-gravity flow beds or tempestite beds because it is rare that all diagnostic lithofacies characteristics can be observed at once. In the case of beds b and c of the sample 2013-5-5 (Fig. 3G), the characteristics are closer to tempestite beds because each bed shows a gradual, consistent fining-upward motif. Regardless, the presence of thin-bedded silty mudstone of either wave-enhanced sediment-gravity flow or tempestite origin in the main phase of the $\delta^{13}C$ excursion clearly indicates that energetic conditions associated with enhanced storm activity were prevalent during the excursion interval, at least on the northwest Panthalassic margin. This interpretation is consistent with the recent observations in western Tethys by Krencker et al. (2015).

5.2.3. Hyperpycnites

As noted in the results section, sandstone hyperpycnites are recognised in the Sakuraguchi-dani succession for the first time (Fig. 2). Cut/polished section analysis of these sandstones reveals key features diagnostic of deposition by hyperpycnal

371 flows. For the sandstone sample 2016-S1-m1.47 (2.6 m section height; Fig. 3H), the
372 lithofacies can be subdivided into three parts: a = massive sandy facies, b = plant-
373 debris-rich poorly sorted sandy facies, and c = faintly laminated silty facies with
374 abundant plant debris (Fig. 3H). According to Yoshida et al. (2009) and Zavala et al.,
375 2011, hyperpycnal flows commonly produce a layer of concentrated terrigenous
376 organic matter in the uppermost part of a hyperpycnite, which is consistent with the
377 observed lithofacies change in 2016-S1-m1.47 (Fig. 3H). This plant matter rich layer
378 emphasises a direct connection between the extra-basinal fluvial system and the
379 depositional environment (Zavala et al., 2011). For the sandstone sample 2016-S1-
380 SST5 (6.4 m section height; Fig. 4), detailed observation reveals that this is a
381 composite sandy bed. The bed is subdivided into four facies: a = massive sandy
382 facies, b = faint, thin finer facies, c = massive sandy facies, and d = laminated silty
383 facies (Fig. 4). These facies differences are supported by grain-size analysis (Fig. 4;
384 Table S2 in supplementary materials). The whole lithofacies characteristics of the
385 sample 2016-S1-SST5 are very similar to those of a specific type of hyperpycnite bed
386 (shown in Fig. 13D in Zavala et al., 2011), which are interpreted to form by a single,
387 long-lived hyperpycnal discharge (Zavala et al., 2011). Furthermore, in sub-facies c
388 (massive sandy facies), a distinct grain-size change was recognised, which is
389 characterized by coarsening upward trend followed by a fining upward trend (Fig. 4;
390 Table S2 in supplementary materials). This grading motif is a key criterion for
391 hyperpycnite identification (Mulder et al., 2003), and reinforces our interpretation that
392 the sample 2016-S1-SST5 is hyperpycnite.
393
394 *5.3. Enhanced hydrological cycling in response to carbon-forced warming*
395

The temporal coincidence between the main phase of the $\delta^{13}C$ excursion and the occurrence of sedimentary features indicative of high-energy conditions and advective transport suggests a causal, climatic link (Figs. 2 and 3). In particular, the concentration of fluid-mud layers and hyperpycnites during the $\delta^{13}C$ excursion, as well as the increase in silt lamina thicknesses, suggests it was an interval of enhanced fluvial discharge. This interpretation is consistent with the postulated increase in terrestrial organic matter and detrital flux inferred from TOC/N and elemental data by Kemp and Izumi (2014). In addition, an increase in storm frequency/intensity, or at least enhanced bottom-water energy conditions, is supported by the concentration of cross laminations, erosive silt layers, silt beds, putative tempestites and wave enhanced sediment gravity flows.

The occurrence of these features within the $\delta^{13}C$ excursion could ostensibly be explained by sea-level fall (e.g. Duarte et al., 2007). However, this possibility is unlikely given the relatively deep water setting of the Nishinakayama Formation compared to the rest of the Toyora Group (Hirano, 1973; Kawamura, 2010), in agreement with the evidence that the Toarcian excursion took place in the context of a worldwide increase and maximum in relative sea level (Hesselbo, 2008 and references therein). Instead, our data suggest a causal link between Toarcian C release and enhanced hydrological cycling. Importantly, this is supported by data from Boreal/Tethyan locations. In Yorkshire, UK, a sudden increase in seawater temperatures inferred from O-isotope and Mg/Ca data, and enhanced global weathering inferred from Os-isotopes, are coeval with the onset of the $\delta^{13}C$ excursion (Bailey et al., 2003; Cohen et al., 2004; Percival et al., 2016; Them et al., 2017a,b). Os-isotope evidence for increased global weathering during the Toarcian event has also recently been provided by Percival et al. (2016) and Them et al. (2017a). Similar

evidence for enhanced hydrological cycling has also been determined from European and Moroccan sections by Ca-isotopes (Brazier et al., 2015) and sedimentology (Hesselbo et al., 2007; Krencker et al., 2015). Our new data from the Panthalassa Ocean margin demonstrate the global nature of this strengthening of the hydrological cycle, facilitated by carbon-forced warming and the consequent effect that this would have on atmospheric water storage and global weather systems (Trenberth, 1999; Bender et al., 2010; Krencker et al., 2015).

6. Conclusions

Our new study of one of the most expanded early Toarcian successions available reveals a rapid decrease in $\delta^{13}C$ correlable with high-resolution records obtained from European successions. Sedimentological data demonstrates a stratigraphic coincidence between rapid carbon emission and a sudden strengthening of the hydrological cycle, which suggests that environmental responses to warming driven by rapid C release were geologically rapid. Our study helps to demonstrate how the enhancement in hydrological cycling during the Toarcian event was globally significant. This perturbation to global climate persisted throughout the main phase of the excursion characterised by minimum $\delta^{13}C$ values, an interval spanning at least 200 k.y. (Suan et al., 2008; Boulila et al., 2014).

Acknowledgements

Part of this work was financially supported by JSPS grants 24-8818 and 15J08821 to KI. DBK acknowledges recipe of NERC Fellowship NE/I02089X/1 and

grants from the Sasakawa Foundation of Great Britain and Daiwa Anglo-Japanese Foundation. This study contributes to IGCP 655. We thank M. Ikeda, T. Ohta, K. Suzuki, N. Nishida and K. Kawano for assistance in the field and/or helpful discussion. Fieldwork was carried out with full permission and support from its landowners. S. Nicoara and S. Kurokawa are thanked for analytical assistance. The comments of the Editor (D. Vance) and three reviewers (G. Suan, S. Bodin, and an anonymous reviewer) greatly improved the manuscript.

Appendix A. Supplementary material

Supplementary materials (one illustration Fig. S1, and two datasheets Table S1 and Table S2) related to this article can be found online at http://dx.doi.org/XX.XXXX/j.epsl.XXXX.XX.XXX.

References

Bailey, T.R., Rosenthal, Y., McArthur, J.M., van de Schootbrugge, B., Thirlwall, M.F., 2003. Paleoceanographic changes of the Late Pliensbachian-early Toarcian interval: a possible link to the genesis of an Oceanic Anoxic Event. Earth Planet. Sci. Lett. 212, 307–320.

Behar, F., Beaumont, V., Penteado, H.L., De B., 2001. Rock-Eval 6 technology: Performance and developments. Oil Gas Sci. Tech. 56, 111–134.

Bender, M.A., Knutson, T.R., Tuleya, R.E., Sirutis, J.J., Vecchi, G.A., Garner, S.T., Held, I.M., 2010. Modeled impact of anthropogenic warming on the frequency of intense hurricanes. Science 327, 454–458.

Boulila, S., Galbrun, B., Huret, E., Hinnov, L.A., Rouget, I., Gardin, S., Bartolini, A., 2014. Astronomical calibration of the Toarcian Stage: Implications for sequence stratigraphy and the duration of the Early Toarcian OAE. Earth Planet. Sci. Lett. 386, 98–111.

Brazier, J-M., Suan, G., Tacail, T., Simon, L., Martin, J.E., Mattioli, E., Balter, V., 2015. Calcium isotope evidence for dramatic increase of continental weathering during the Toarcian oceanic anoxic event (Early Jurassic). Earth Planet. Sci. Lett. 411, 164–176.

Cohen, A.S., Coe, A.L., Harding, S.M., Schwark, L., 2004. Osmium isotope evidence for the regulation of atmospheric CO_2 by continental weathering. Geology 32, 157–160.

Dalrymple, R.W., Baker, E.K., Harris, P.T., Hughes, M.G., 2003. Sedimentology and stratigraphy of a tide-dominated, foreland-basin delta (Fly River, Papua New Guinea), in: Sidi, F.H., Nummedal, D., Imbert, P., Darman, H., Posamentier, H.W. (Eds.), Tropical Deltas of Southeast Asia—Sedimentology, Stratigraphy, and Petroleum Geology. SEPM Special Publication 76, pp. 147–173.

Duarte, L.V., Oliveira, L.C., Rodigues, R., 2007. Carbon isotopes as a sequence stratigraphic tool: examples from the Lower and Middle Toarcian marly limestones of Portugal. Bol. Geol. Min. España. 118, 3–18.

Faas, R.W., 1991. Rheological boundaries of mud: Where are the limits? Geo-Mar. Lett. 11, 143–146.

Hermoso, M., Minoletti, F., Rickaby, R.E.M., Hesselbo, S.P., Baudin, F., Jenkyns, H.C., 2012. Dynamics of a stepped carbon-isotope excursion: Ultra high-resolution study of Early Toarcian environmental change. Earth Planet. Sci. Lett. 319–320, 45–54.

Hesselbo, S.P., 2008. Sequence stratigraphy and inferred relative sea-level change from the onshore British Jurassic. P. Geologists. Assoc. 119, 19–34.

Hesselbo, S.P., Pienkowski, G., 2011. Stepwise atmospheric carbon-isotope excursion during the Toarcian Oceanic Anoxic Event (Early Jurassic, Polish Basin). Earth Planet. Sci. Lett. 301, 365–372.

Hesselbo, S.P., Gröcke, D.R., Jenkyns, H.C., Bjerrum, C.J., Farrimond, P., Morgans Bell, H.S., Green, O.R., 2000. Massive dissociation of gas hydrate during a Jurassic oceanic event. Nature 406, 392–395.

517 Hesselbo, S.P., Morgans-Bell, H.S., McElwain, J.C., Rees, P.M., Robinson, S.A.,
518 Ross, C.E., 2003. Carbon-cycle perturbation in the Middle Jurassic and accompanying
519 changes in the terrestrial paleoenvironment. J. Geol. 111, 259–276.
520
521 Hesselbo, S.P., Jenkyns, H.C., Duarte, L.V., Oliveira, L.C.V., 2007. Carbon-isotope
522 record of the Early Jurassic (Toarcian) Oceanic Anoxic Event from fossil wood and
523 marine carbonate (Lusitanian Basin, Portugal). Earth Planet. Sci. Lett. 253, 455–470.
524
525 Hill, P.S., Fox, J.M., Crockett, J.S., Curran, K.J., Friedrichs, C.T., Geyer, W.R.,
526 Milligan, T.G., Ogston, A.S., Puig, P., Scully, M.E., Traykovski, P.A., Wheatcroft,
527 R.A., 2007. Sediment delivery to the seabed on continental margins, in: Nittrouer,
528 C.A., Austin, J.A., Field, M.E., Kravitz, J.H., Syvitski, J.P.M., Wiberg, P.L. (Eds.),
529 Continental Margin Sedimentation: From Sediment Transport to Sequence
530 Stratigraphy. International Association of Sedimentologists Special Publication 37, pp.
531 49–99.
532
533 Hirano, H., 1973. Biostratigraphic study of the Jurassic Toyora Group, part 3. Trans.
534 Proc. Palaeont. Soc. Japan, N.S. 90, 45–71.
535
536 Ichaso, A.A., Dalrymple, R.W., 2009. Tide- and wave-generated fluid mud deposits in
537 the Tilje Formation (Jurassic), offshore Norway. Geology 37, 539–542.
538
539 Izumi, K., Miyaji, T., Tanabe, K., 2012. Early Toarcian (Early Jurassic) oceanic
540 anoxic event recorded in the shelf deposits in the northwestern Panthalassa: evidence
541 from the Nishinakayama Formation in the Toyora area, west Japan. Palaeogeogr.

542 Palaeoclimatol. Palaeoecol. 315–316, 100–108.

543

544 Izumi, K., Suzuki, R., Inui, M., 2017. Estimating the degree of mudstone
545 compactional thinning: Empirical relationship between mudstone compaction and
546 geochemical composition. Trans. Kokushikan Univ. Sci. Eng., Tokyo, Japan 10, 29–
547 37.

548

549 Jenkyns, H.C., Gröcke, D.R., Hesselbo, S.P., 2001. Nitrogen isotope evidence for
550 water mass denitrification during the early Toarcian (Jurassic) oceanic anoxic event.
551 Palaeoceanography 16, 593–603.

552

553 Kawamura, H., 2010. Stratigraphic revision of the Jurassic Toyora Group of the
554 southern part of the Tabe Basin, Yamaguchi Prefecture, southwest Japan. Jour. Geol.
555 Soc. Japan 116, 27–44. (in Japanese with English abstract)

556

557 Kemp, D.B., Izumi, K., 2014. Multiproxy geochemical analysis of a Panthalassic
558 margin record of the early Toarcian oceanic anoxic event (Toyora area, Japan).
559 Palaeogeogr. Palaeoclimatol. Palaeoecol. 414, 332–341.

560

561 Kemp, D.B., Coe, A.L., Cohen, A.S., Schwark, L., 2005. Astronomical pacing of
562 methane release in the Early Jurassic period. Nature 437, 396–399.

563

564 Kemp, D.B., Coe, A.L., Cohen, A.S., Weedon, G.P. 2011. Astronomical forcing and
565 chronology of the Early Toarcian (Early Jurassic) Oceanic Anoxic Event in
566 Yorkshire, UK. Paleoceanography 26, PA4210.

Krencker, F-N., Bodin, S., Suan, G., Heimhofer, U., Kabiri, L., Immenhauser, A., 2015. Toarcian extreme warmth led to tropical cyclone intensification. Earth Planet. Sci. Lett. 425, 120–130.

Lazar, O.P., Bohacs, K.M., Schieber, J., Macquaker, J.H.S., Demko, T.M., 2015. Mudstone Primer: Lithofacies variations, diagnostic criteria, and sedimentologic-stratigraphic implications at lamina to bedset scales. SEPM Concepts in Sedimentology and Paleontology 12, 198 p.

Macquaker, J.H.S., Bentley, S.J., Bohacs, K., Lazar, R., Jonk, R., 2010. Wave-enhanced sediment-gravity flows and mud dispersal across continental shelves: Reappraising sediment transport processes operating in ancient mudstone successions. Geology 38, 947–950.

McElwain, J.C., Wade-Murphy, J., Hesselbo, S.P., 2005. Changes in carbon dioxide during an oceanic anoxic event linked to intrusion into Gondwana coals. Nature 435, 479–482.

Mulder, T., Alexander, J., 2001. The physical character of subaqueous sedimentary density flows and their deposits. Sedimentology 48, 269–299.

Mulder, T., Migeon, S., Savoye, B., Faugeres, J.-C., 2001. Inversely graded turbidite sequences in the deep Mediterranean. A record of deposits from flood-generated turbidity currents? Geo-Mar. Lett. 21, 86–93.

Mulder, T., Syvitski, J.P.M., Migeon, S., Faugeres, J.-C., Savoye, B., 2003. Marine hyperpycnal flows: initiation, behavior and related deposits. A review. Mar. Petrol. Geol. 20, 861–882.

Nakada, K., Matsuoka, A., 2011. International correlation of the Pliensbachian/Toarcian (Lower Jurassic) ammonoid biostratigraphy of the Nishinakayama Formation in the Toyora Group, southwest Japan. Newsl. Stratigr. 44, 89–111.

Nishida, N., Ito, M., 2009. Fluid mud: Distinctive features and implications for genetic stratigraphy. Jour. Geol. Soc. Japan 115, 149–167 (in Japanese with English abstract).

Nishida, N., Ito, M., Inoue, A., Takizawa, S., 2013. Clay fabric of fluid-mud deposits from laboratory and field observations: Potential application to the stratigraphic record. Mar. Geol. 337, 1–8.

Percival, L.M.E., Cohen, A.S., Davies, M.K., Hesselbo, S.P., Jenkyns, H.C., Leng, M.J., Mather, T.A., Storm, M.S., Xu, W. 2016. Osmium isotope evidence for two pulses of increased continental weathering linked to Early Jurassic volcanism and climate change. Geology 44, 759–762.

615 Röhl, H.-J., Schmid-Röhl, A., 2005. Lower Toarcian (Upper Liassic) black shales of
616 the Central European Epicontinental Basin: A sequence stratigraphic case study from
617 the SW German Posidonia Shale. SEPM Spec. Publ. 82, 165–189.
618
619 Ruebsam, W, Münzberger, P., Schwark, L., 2014. Chronology of the Early Toarcian
620 environmental crisis in the Lorraine Sub-Basin (NE Paris Basin). Earth Planet. Sci.
621 Lett. 404, 273–282.
622
623 Suan, G., Pittet, B., Bour, I., Mattioli, E., Duarte, L.V., Mailliot, S., 2008. Duration of
624 the Early Toarcian carbon isotope excursion deduced from spectral analysis:
625 consequence for its possible causes. Earth Planet. Sci. Lett. 267, 666–679.
626
627 Suan, G., van de Schootbrugge, B., Adatte, T., Fiebig, J., Oschmann, W., 2015.
628 Calibrating the magnitude of the Toarcian carbon cycle perturbation.
629 Paleoceanography 30, 495–509.
630
631 Svensen, H., Planke, S., Chevallier, L., Malthe-Sorenssen, A., Corfu, F., Jamtveit, B.,
632 2007. Hydrothermal venting of greenhouse gases triggering Early Jurassic global
633 warming. Earth Planet. Sci. Lett. 256, 554–566.
634
635 Tanabe, K., Inazumi, A., Ohtsuka, Y., Katsuta, T., Tamahama, K., 1982. Litho- and
636 biofacies and chemical composition of the Lower Jurassic Nishinakayama Formation
637 (Toyora Group) in west Japan. Ehime Univ. Mem. Sci. Ser. D 9, 47–62. (in Japanese
638 with English abstract)
639

Them, T.R., Gill, B.C., Selby, D., Gröcke, D.R., Friedman, R.M., Owens, J.D., 2017a. Evidence for rapid weathering response to climatic warming during the Toarcian Oceanic Anoxic Event. Sci. Rep. 7, 5003.

Them, T.R., Gill, B.C., Caruthers, A.H., Gröcke, D.R., Tulsky, E.T., Martindale, R.C., Poulton, T.P., Smith, P.L., 2017b. High-resolution carbon isotope records of the Toarcian Oceanic Anoxic Event (Early Jurassic) from North America and implications for the global drivers of the Toarcian carbon cycle. Earth Planet. Sci. Lett. 459, 118–126.

Trenberth, K., 1999. Conceptual framework for changes of extremes of the hydrologic cycle with climate change. Climatic Change 42, 327–339.

Tyson, R.V., 1995. Bulk Geochemical Characterization and Classification of Organic Matter: Elemental Analysis and Pyrolysis, in: Sedimentary Organic Matter: Organic facies and palynofacies. Springer Netherlands, Dordrecht, pp. 367–382.

Wells, J.T., 1995. Tide-dominated estuaries and tidal rivers, in: Perillo, G.M.E. (Ed.), Geomorphology and Sedimentology of Estuaries. Elsevier, Amsterdam, pp. 179–205.

Yoshida, K., Kawakami, G., Kawamura, M., 1995. Heavy mineral-concentrated sandstones in the Upper Permian and the Lower Triassic of the South Kitakami Terrane. Jour. Geol. Soc. Japan 101, 279–294. (in Japanese with English abstract)

Yoshida, M., Yoshiuchi, Y., Hoyanagi, K., 2009. Occurrence conditions of hyperpycnal flows, and their significance for organic-matter sedimentation in a Holocene estuary, Niigata Plain, Central Japan. Isl. Arc 18, 320–332.

Zavala, C., Arcuri, M., Meglio, M. Di, Gamero Diaz, H., Contreras, C., 2011. A genetic facies tract for the analysis of sustained hyperpycnal flow deposits, in: Slatt, R. M., Zavala, C. (Eds.), Sediment transfer from shelf to deep water—Revisiting the delivery system. AAPG Studies in Geology 61, pp. 31–51.

Figure captions

Figure 1 | Palaeogeography of the Early Jurassic and locations of Early Toarcian deposits. Note the European bias in study locations. Inset, location map of the Sakuraguchi-dani stream valley succession in Yamaguchi Prefecture, Japan. Sakuraguchi-dani location map and palaeogeographic reconstruction redrawn from Cohen et al. (2004) and Kemp and Izumi (2014).

Figure 2 | Sedimentary log with $\delta^{13}C$ and sedimentological data through the Sakuraguchi-dani succession. Organic $\delta^{13}C$ data for bulk mudstone and wood are shown. These data delineate a ~30 m thick negative excursion in $\delta^{13}C$ of ~3‰ divided into a main phase (blue shading) and recovery interval (purple shading). Mudstone $\delta^{13}C$ data below ~5 m and above ~0 m are from Kemp and Izumi (2014; see Table S1 in supplementary materials for full data listing). The onset of the shift to minimum $\delta^{13}C$ values is stepped, comprising two separate abrupt shifts (labeled A and B). Shift A straddles an inferred fault (brecciated interval; see text for details). Occurrences of

689 sedimentary features indicative of high-energy/advective transport are concentrated in
690 the main phase. Silt laminae are generally thicker during the main phase. Ammonite
691 zones are from Nakada and Matsuoka (2011).
692
693 **Figure 3** | Images of key sedimentary features in silty mudstones facies. All images
694 taken perpendicular to bedding planes. (A) Thin-section photomicrograph of parallel-
695 laminated silty mudstone (-13.62 m section height), suggesting a quiescent and likely
696 dysoxic environment. (B) Thin-section photomicrograph of bioturbated silty
697 mudstone (-12.72 m). Note the presence of *Phycosiphon* (arrows). (C) Thin-section
698 scan image of ripple cross-laminated silty mudstone (8.90 m). (D) Thin-section scan
699 image of silty mudstone showing presence of homogeneous muddy layer (-2.00 m).
700 (E) Magnified thin-section photomicrograph of homogenous muddy layer in D. This
701 layer is characterized by sharp layer contacts, absence of internal lamination, rare
702 bioturbation, and randomly scattered amorphous organic matter. This layer is
703 interpreted as a compacted fluid-mud deposit layer (see main text). (F) Thin-section
704 scan image of silty mudstones showing the presence of two (nearly amalgamated) silt
705 beds likely indicative of traction transport (2.10 m). Note that faint internal laminae
706 are recognised within these silt beds. (G) Thin-section scan image of thin-bedded silty
707 mudstone (1.00 m). At least three independent beds are recognised: a = homogeneous
708 muddy bed, which may be interpreted as a fluid-mud deposit layer, b and c = silty
709 beds with basal internal laminae showing gradual lithological change (fining upward
710 trend), which may be interpreted as storm-associated tempestites or wave-enhanced-
711 sediment-gravity-flows (see also supplementary materials). (H) Scan image of cut
712 surface of sandstone bed (2.6 m), which is subdivided into three facies: a = massive
713 sandy facies, b = plant-debris-rich poorly sorted sandy facies, and c = faintly

laminated silty facies with abundant plant debris. This sandstone is interpreted as a hyperpycnite (see also supplementary materials). (I) Scan image of cut surface of sandstone bed interpreted as a debrite (6.10 m). Note the presence of randomly scattered mud clasts (arrows).

Figure 4 | Scan image of the sandstone sample (2016-S1-SST5; 6.4 m), with graph showing the internal grain-size variations and representative thin-section photomicrographs of each horizon. This sample is subdivided into four lithofacies (a to d in the left photograph; see text for detail). Note the characteristic grain-size variation, suggesting that this bed was formed by a hyperpycnal flow (see main text for details).

Figure 5 | Correlation of Sakuraguchi-dani and European $\delta^{13}C$ records. Records are plotted on the same relative stratigraphic thickness and excursion magnitude scale (shift B = 0 m). This plot helps to highlight the great relative thickness of the Sakuraguchi-dani $\delta^{13}C$ profile relative to European $\delta^{13}C$ profiles. Data are correlated based on the presence of at least 2 stratigraphically abrupt $\delta^{13}C$ shifts in all the successions (green and purple dashed lines). In some records, and in the accompanying publications, a 3rd shift has also been noted/suggested (blue dashed line). Evidence for a 3rd shift in the Sakuraguchi-dani record is somewhat equivocal, though the general morphology of the $\delta^{13}C$ record is very similar to that recorded in Portugal (Peniche section). Correlation between the UK (Yorkshire section) $\delta^{13}C$ profile and the Portuguese profile is based on Kemp et al. (2011). Correlation of the Polish $\delta^{13}C$ (Brody-Lubienia section) terrestrial phytoclast record with the UK profile is based on Hesselbo and Pienkowski (2011). Italian $\delta^{13}C$ inorganic and organic $\delta^{13}C$

739 data are from the Belluno Trough section. The German $\delta^{13}C$ profile is from the
740 Denkingen borehole. Inorganic and organic $\delta^{13}C$ data in the French profile are from
741 the Sancerre borehole (all references are on figure). The termination of the excursion
742 in each record is shown by the red dashed line.

Figure 1

Click here to download Figure: izumi_etal_figure 1.pdf

Izumi et al. (2017) - Figure 1

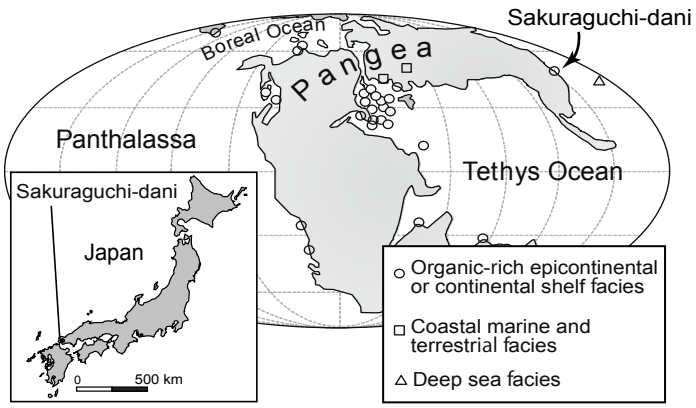

Figure 2

Click here to download Figure: izumi_etal_figure 2_revised.pdf

Izumi et al. (2017) - Figure 2

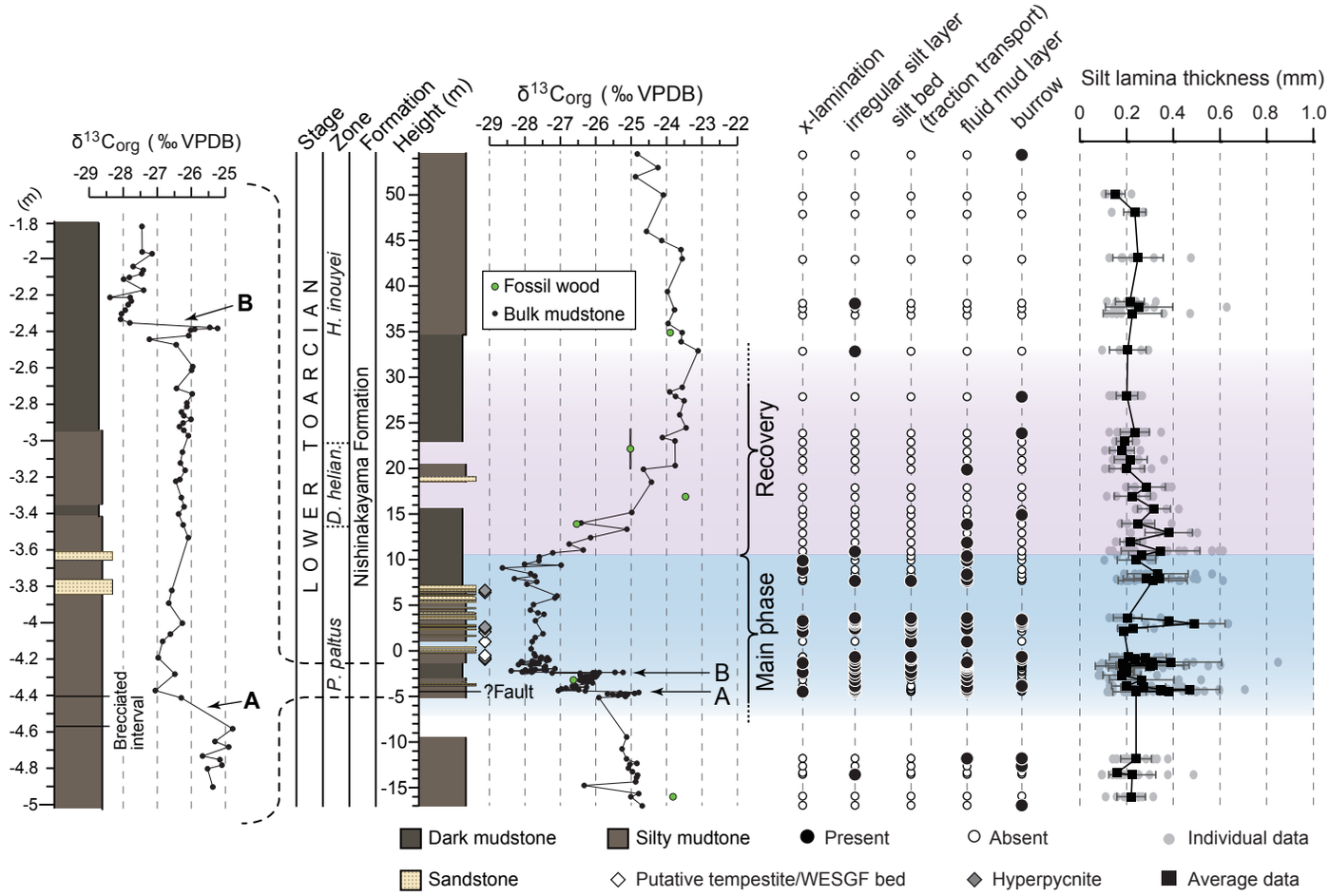

Figure 3

Click here to download high resolution image

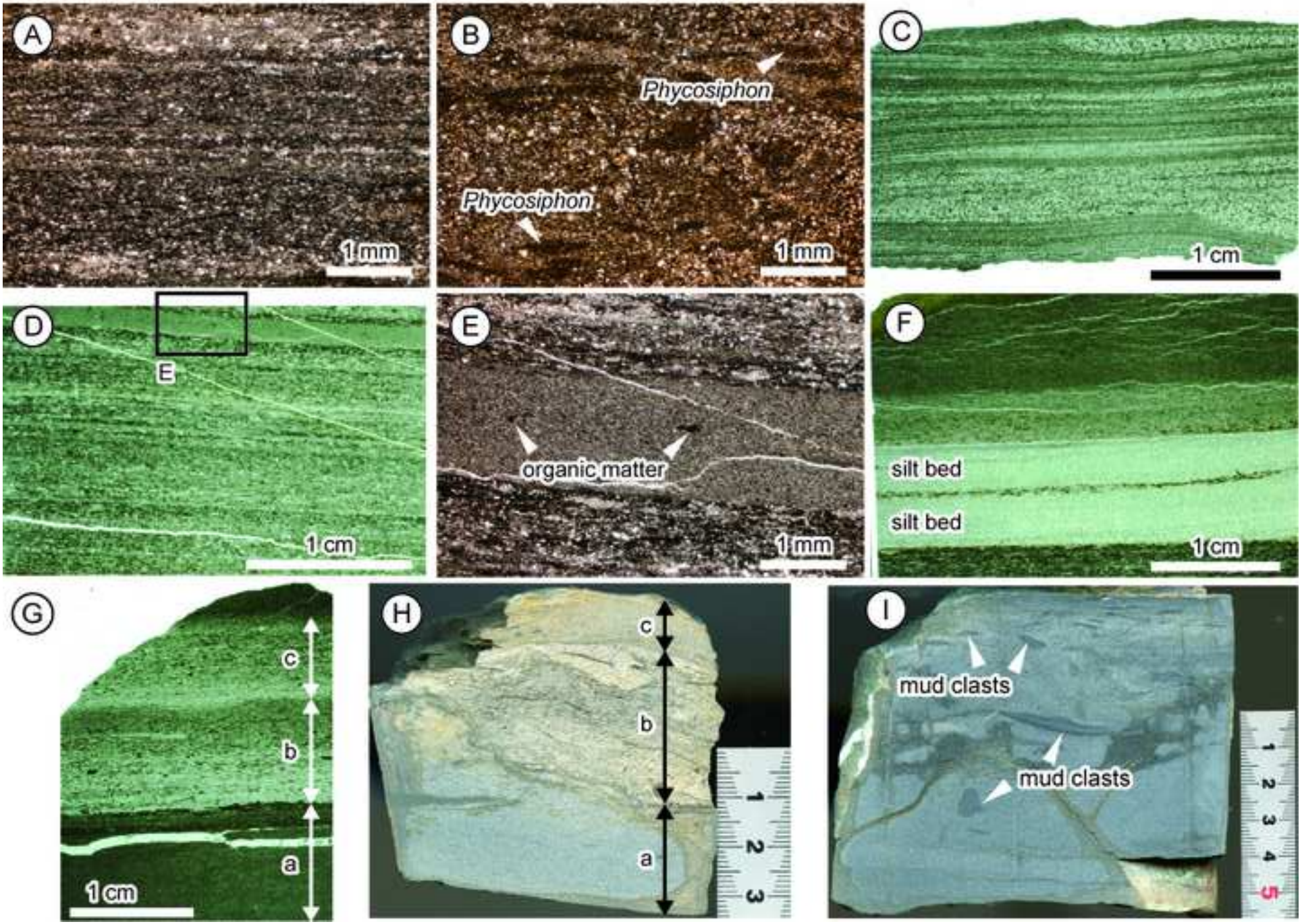

Figure 4

Click here to download high resolution image

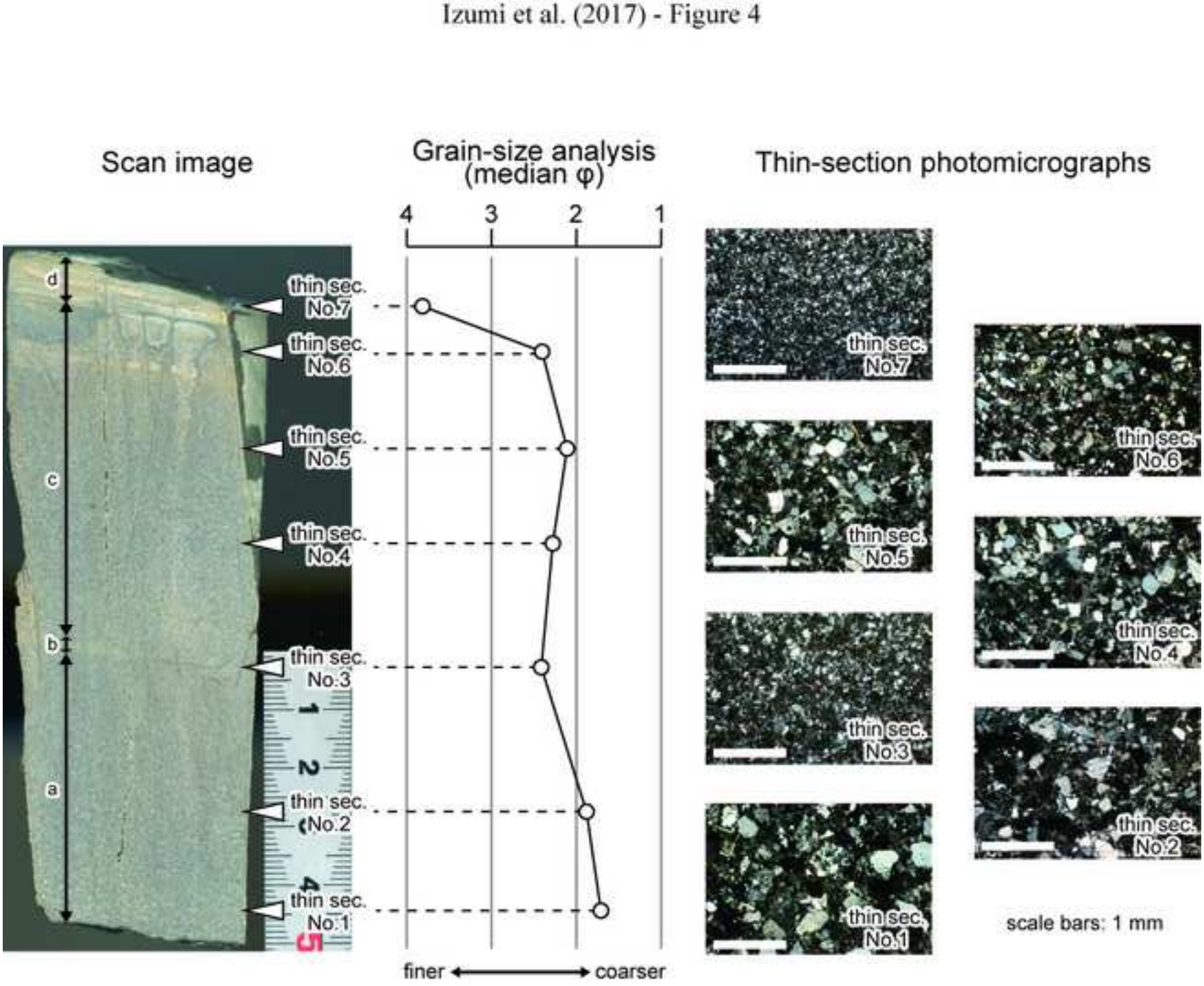

Figure 5

Click here to download Figure: izumi_etal_new figure 5 (original figure 6 revised).pdf

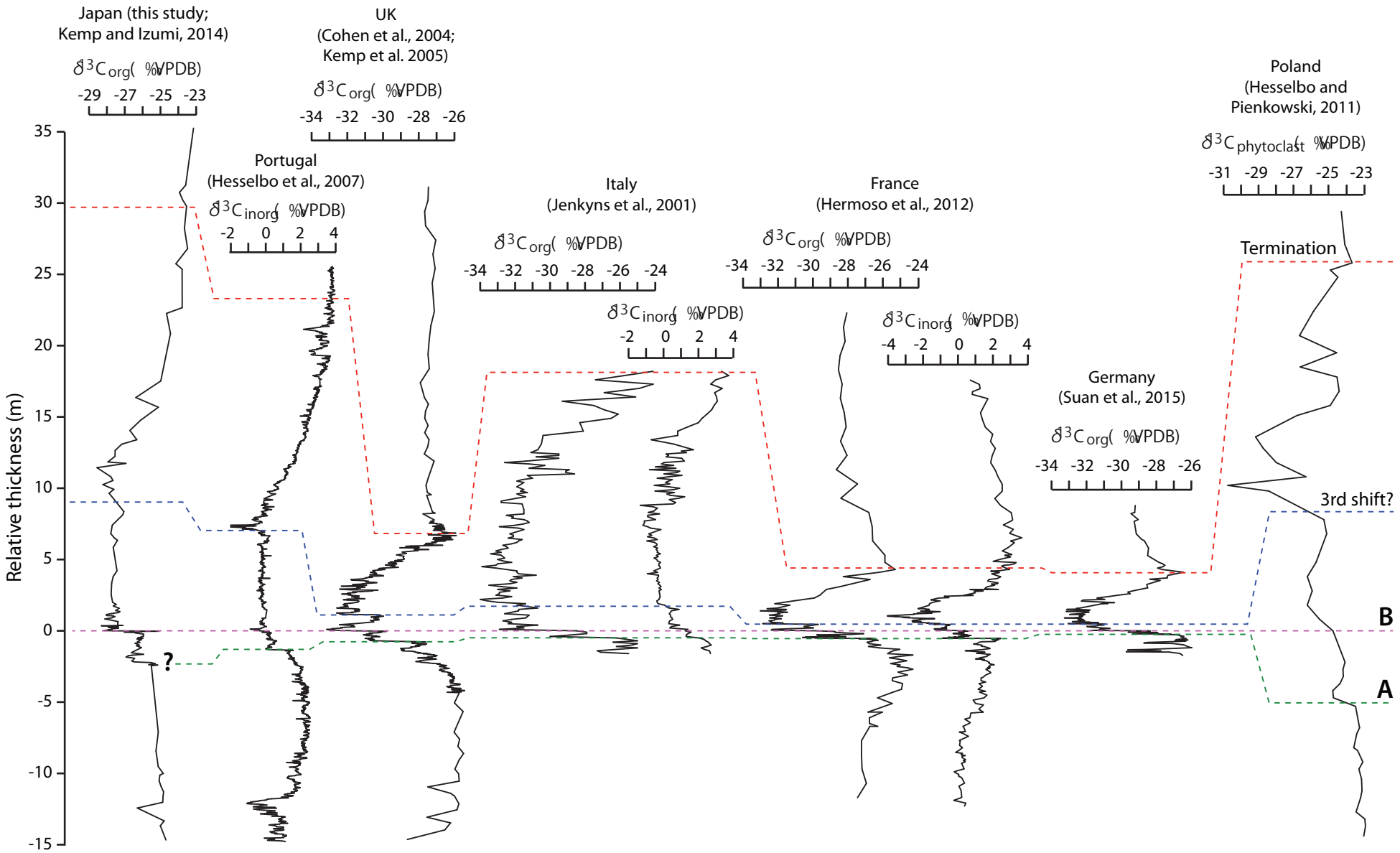

Izumi et al. (2017) - Figure 5

Figure 3 (high-resolution)

Click here to download Figure (high-resolution): izumi_etal_new figure 3 (originally figure 4)_high resolution.tif

Figure 4 (high-resolution)

Click here to download Figure (high-resolution): izumi_etal_new figure 4 (originally figure 5)_high resolution.tif

Table S1

Click here to download Supplementary material for online publication only: izumi_etal_table S1.xlsx

Table S2

Click here to download Supplementary material for online publication only: izumi_etal_table S2.xlsx

Figure S1

Click here to download Supplementary material for online publication only: izumi_etal_figure S1.pdf